catalysts

MDPI

Review

Engineering Covalent Organic Frameworks for Photocatalytic CO_2 Reduction: From Exciton Dissociation to Product Selectivity

Dingming Xue [1,2], Bing Ma [1,2], Xiuzhen Fan [3], Lei Jiang [1], Ning Su [4,*], Xiaodong Li [1,2,*], Changchun Yan [1,2,*] and Hao Zhou [1,2,*]

[1] Nanjing Institute of Environmental Sciences, Ministry of Ecology and Environment, Nanjing 210042, China; xue_dingming@nies.org (D.X.)
[2] East China Regional Technology Center of Hazardous Waste Environmental Risk Prevention and Control, Nanjing 210042, China
[3] Shandong Haipuou Environmental Protection Equipment Technology Co., Ltd., Zhucheng 262200, China
[4] College of Mechanical Engineering, Ningbo University of Finance and Economics, Ningbo 315175, China
* Correspondence: suning@nbufe.edu.cn (N.S.); lixiaodong@nies.org (X.L.); y19801286607@163.com (C.Y.); zhouhao@nies.org (H.Z.)

Abstract

Solar-driven CO_2 reduction requires a photocatalyst to integrate light harvesting, exciton dissociation, long-range charge transport, CO_2 adsorption and activation, and multielectron proton-coupled electron transfer within a single structural platform. Covalent organic frameworks (COFs) are attractive in this context because their π-conjugated backbones, periodic pores, linkage chemistry, stacking modes, and catalytic sites can be programmed with molecular precision. Nevertheless, the literature remains dominated by phenomenological correlations between optical response and product yield, while the causal relationships among exciton binding energy (E_b), free-carrier generation, interfacial charge transfer, intermediate adsorption, and product selectivity remain insufficiently resolved. This review develops a unified structure–activity framework in which intrinsic π-conjugation and donor–acceptor polarization regulate E_b and exciton diffusion; morphology and heterojunctions control the competition between interfacial transfer and recombination; and active-site coordination and pore microenvironments determine local electron density, proton delivery, and the adsorption energies of *COOH, *OCHO, *CO, *CHO, and *OCCO intermediates. Representative performance is benchmarked only when $^{13}CO_2$ isotope tracing and appropriate blank controls are available, with external homogeneous photosensitizer systems treated separately. Among the entries retained in the condition-aware benchmark, reported CO production rates span 17.75–20,110 μmol g^{-1} h^{-1} and wavelength-specific AQYs span 0.058–5.1%; these values are not directly comparable without the associated photon flux, reactor configuration, catalyst loading, and auxiliary components. Finally, operando spectroscopy, density functional theory, microkinetic modelling, stability analysis, standardized reporting, machine-learning-assisted discovery, and device-oriented scale-up are discussed as routes toward predictive and reproducible COF photocatalyst engineering.

Keywords: covalent organic frameworks; CO_2 photoreduction; exciton binding energy; product selectivity; in situ characterization

Academic Editor: Akira Nishimura

Received: 31 July 2026
Revised: 24 September 2026
Accepted: 29 September 2026
Published: 14 October 2026

Copyright: © 2026 by the authors. Licensee MDPI, Basel, Switzerland. This article is an open access article distributed under the terms and conditions of the Creative Commons Attribution (CC BY) license.

1. Introduction

1.1. Solar-Driven CO_2 Photoreduction: Background and Thermodynamic/Kinetic Challenges

The conversion of carbon dioxide into carbon monoxide, formic acid, methanol, methane, and multicarbon products offers a conceptually direct route to coupling carbon recycling with solar energy storage. In contrast to simple one-electron photochemistry, however, CO_2 reduction is a network of proton-coupled electron-transfer reactions whose branches differ in electron number, proton demand, intermediate stability, and desorption kinetics. The first activation of linear, thermodynamically stable CO_2 is intrinsically difficult; subsequent steps must compete with back-electron transfer, surface poisoning, and hydrogen evolution. Product formation, therefore, depends not only on whether a conduction-band electron is sufficiently reducing but also on whether a usable population of free electrons can be generated, transported, and delivered to a chemically competent site on the timescale required for sequential reduction. Recent analyses of selectivity emphasize that nominal band-edge potentials alone cannot predict product distributions because adsorption free energies, proton activity, local electric fields, and the lifetime of reducing equivalents collectively reshape the accessible reaction network [1].

CO_2 conversion is pursued through complementary thermochemical, electrochemical, and photochemical routes. Thermochemical catalysis commonly uses heat, pressure, or a co-reactant; electrochemical reduction controls electron delivery through an applied potential; and photocatalysis couples light absorption to surface redox chemistry. Metal–organic frameworks (MOFs) and covalent organic frameworks (COFs) both offer tunable pores and adsorption environments [2–4]. This review focuses on COFs because their covalently connected organic chromophores allow linkage polarity, intralayer conjugation, and interlayer coupling to be varied together with catalytic-site coordination. They therefore provide a useful platform for examining how bound excitons become reactive carriers and how those carriers feed competing CO_2-reduction pathways. This scope does not imply that MOFs are intrinsically less effective; quantitative comparisons are restricted to COF-based photocatalysis because the driving forces and rate descriptors differ across conversion routes.

An additional complication arises from the electronic nature of organic semiconductors. Photoabsorption in a COF generally produces a coulombically bound electron-hole pair rather than two immediately independent carriers. This bound state is an exciton. Its dissociation must compete with radiative and nonradiative decay, exciton trapping, and interlayer excimer formation before free electrons and holes can drive surface reactions. Consequently, a material may display broad visible-light absorption yet still deliver low catalytic activity when its exciton binding energy (E_b) is high, its dielectric screening is weak, or the distance between the exciton-generation domain and the catalytic interface exceeds the exciton diffusion length. The importance of excitonic effects in COFs has been established through ultrafast measurements and theory, including observations of rapid charge separation in ordered donor-acceptor heterojunctions [5], domain-size-dependent exciton transport [6], and chemically tunable exciton dissociation in donor-acceptor frameworks [7,8]. These findings require photocatalytic CO_2 reduction to be described as a sequence of coupled photophysical and catalytic events rather than as a single band-to-band electron-transfer process.

https://doi.org/10.3390/catal16100909

The kinetic demands become progressively more severe as the depth of reduction increases. CO formation is commonly described through *COOH generation followed by *CO formation and desorption, whereas formate production is associated with an *OCHO-type branch. Methane formation requires sustained multielectron and multiproton delivery, and C_{2+} synthesis additionally requires the spatial and temporal coincidence of carbonaceous intermediates for C-C coupling. At the same time, protons and photogenerated electrons can be consumed by hydrogen evolution. A dynamic competition among CO_2 adsorption, proton adsorption, intermediate hydrogenation, C-C coupling, desorption, and charge recombination thus governs selectivity. The central design problem is not simply to maximize charge separation or CO_2 uptake in isolation, but to synchronize free-carrier supply with the chemical requirements of the desired pathway.

1.2. Intrinsic Structural Advantages of COFs for Photocatalysis

COFs provide an unusual degree of control over this synchronization. Since their first demonstration as porous crystalline polymers [9], COFs have evolved into modular semiconducting frameworks in which chromophores, electron donors and acceptors, polar groups, metal-binding ligands, and catalytic centers can be positioned periodically. The backbone determines the optical gap and intraframework delocalization; the linkage controls conjugation, dipole orientation, and chemical stability; the stacking geometry regulates interlayer coupling and charge migration; and the pore wall defines the adsorption microenvironment. This modularity allows photophysical and catalytic functions to be integrated into a single ordered material rather than assembled as weakly coupled components.

The mechanistic value of COFs lies in separating structural variables that are often coupled in less ordered organic photocatalysts. Ethynyl extension changes intraframework conjugation and carrier delivery [10], whereas reversing imine connectivity tests how linkage orientation changes exciton localization without changing the nominal framework composition [11]. Interlayer decoupling and twisted stacking address a different bottleneck: whether charges can leave the photoexcited domain without being lost through interlayer recombination [12,13]. Dimensional isomerism and quasi-one-dimensional frameworks further change the distance and connectivity between light-harvesting units and accessible sites [14,15]. At the reaction centre, La-Ni motifs and Rh-containing frameworks link metal coordination to *COOH formation and CO release [16,17]. These comparisons motivate a structure-activity analysis in which improved absorption, productive charge separation, and selective surface chemistry are tested as distinct steps.

1.3. Critical Bottlenecks of COF-Based CO_2 Photocatalysis

Despite rapid progress, four bottlenecks remain. First, E_b is still rarely measured or calculated in a form that can be compared across frameworks. Photoluminescence quenching and increased photocurrent are often interpreted as evidence of improved charge separation, but neither observation uniquely quantifies exciton dissociation. Second, charge-transfer pathways are often inferred from static band diagrams, even though transfer and recombination occur over femtosecond-to-millisecond timescales. Third, catalytic selectivity is often discussed independently of photophysics, creating a logical gap between a material that produces more carriers and a site that selects a particular reaction branch. Fourth, performance comparisons remain vulnerable to inconsistent catalyst mass, reactor geometry, light intensity, product normalization, sacrificial-agent use, cocatalyst loading, and incomplete carbon-source validation. Isotope-tracer studies have demonstrated that contamination from residual carbon species, solvents, or catalyst decomposition can produce misleading signals unless $^{13}CO_2$ experiments and rigorous blanks are designed correctly [18].

https://doi.org/10.3390/catal16100909

These weaknesses are particularly consequential for claims of deep reduction and C_{2+} formation, where trace products can be overinterpreted, and carbon balances are difficult to assess. A credible benchmark should report the exact light spectrum and irradiance, reaction phase, catalyst loading, CO_2 concentration, proton source, sacrificial reagent, photosensitizer, and cocatalyst, product-detection method, selectivity definition, and apparent quantum yield (AQY). It should also demonstrate product origin through $^{13}CO_2$ labeling and include no-light, no-catalyst, and no-CO_2 or inert-gas controls. Systems that require external homogeneous photosensitizers are scientifically informative, especially for active-site chemistry, but should not be directly compared with self-photosensitizing COFs because the sites of photon absorption and primary charge generation differ.

1.4. Scope and Core Focus of This Review

This review focuses on intrinsic COFs and COF-based composites that function as heterogeneous photocatalysts for CO_2 reduction. Systems dominated by an additional homogeneous photosensitizer are discussed only when they provide mechanistic insight and are excluded from the strict performance benchmark. Noble-metal-containing materials are retained but explicitly identified. The analysis is organized around a causal chain: π-conjugated skeleton engineering and polarization regulate E_b and exciton diffusion; exciton dissociation generates free carriers; morphology, built-in fields, and interfaces determine whether those carriers reach catalytic sites before recombination; the local electronic structure and pore microenvironment then control CO_2 adsorption, reaction barriers, and intermediate lifetimes; finally, these factors determine turnover and product selectivity. This perspective places quantitative mechanisms of exciton control and selectivity within a single structure-activity relationship rather than treating them as separate topics.

Positioning relative to recent reviews. Earlier reviews established COFs as programmable platforms for CO_2 photoreduction [19], while later perspectives emphasized active-site engineering [20], linkage chemistry [21], or heterostructure construction [22]. Building on these foundations, this review uses a stricter causal organization—E_b → free-carrier generation → interfacial transfer → active-site/intermediate energetics → product selectivity—and couples it to isotope- and condition-aware benchmarking. This distinction is intended to expose where a reported activity originates, rather than to rank material classes by a single rate value.

2. Fundamentals of COF-Based CO_2 Photoreduction: Exciton Behavior and Catalytic Pathways

2.1. Basic Reaction Chain of Photocatalytic CO_2 Reduction

A complete COF photocatalytic cycle can be divided into six coupled stages: photon absorption and exciton generation; exciton diffusion and dissociation; migration of free carriers through the framework; interfacial transfer to oxidation and reduction sites; CO_2 adsorption and multistep proton-coupled electron transfer; and product desorption with catalyst regeneration. The distinction between an exciton and a free carrier is fundamental. An exciton is a correlated electron-hole pair stabilized by coulomb attraction. It can transport excitation energy and, in some cases, participate in energy-transfer chemistry. However, surface reduction requires an electron that is sufficiently separated from its hole to act as a charge carrier. Accordingly, the population relevant to CO_2 reduction is determined by the quantum yield of exciton dissociation and by the fraction of the resulting electrons that survive transport to an active site.

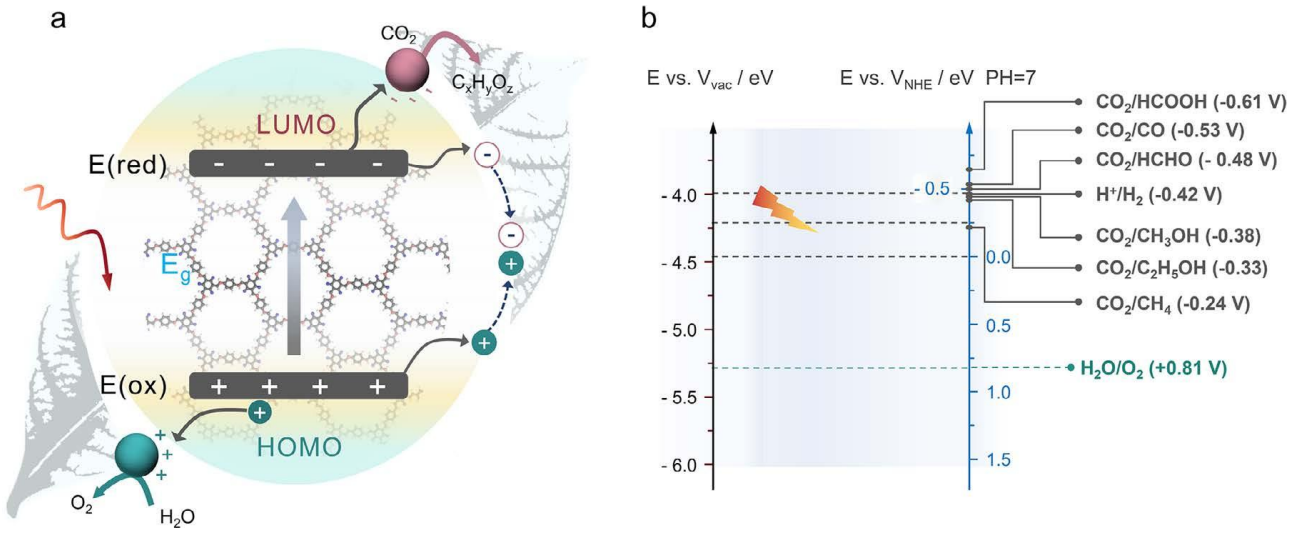
The product-specific reduction half-reactions provide stoichiometric constraints: $CO_2 + 2H^+ + 2e^- \rightarrow CO + H_2O$; $CO_2 + 2H^+ + 2e^- \rightarrow HCOOH$; $CO_2 + 8H^+ + 8e^- \rightarrow CH_4 + 2H_2O$; and $2CO_2 + 12H^+ + 12e^- \rightarrow C_2H_4 + 4H_2O$. When water supplies the reducing equivalents, the coupled oxidation half-reaction is $2H_2O \rightarrow O_2 + 4H^+ + 4e^-$; competing proton reduction follows $2H^+ + 2e^- \rightarrow H_2$. These are balanced half-reactions rather than elementary mechanisms. Surface conversion proceeds through adsorbed species such as $*CO_2^-$, *COOH, *OCHO, *CO, *CHO, and *OCCO, whose formation and consumption depend on the catalytic site and proton-coupled electron transfer (PCET).

Following light absorption, the initial excited state may remain localized on one chromophore, delocalize along a conjugated segment, form an interlayer excimer, or undergo intramolecular charge transfer in a donor-acceptor framework. The electronic coupling between building blocks, torsional disorder, linkage polarity, layer registry, dielectric environment, and energetic offsets control these pathways. Ordered donor-acceptor COFs can create nanoscale heterojunctions in which charge separation occurs on ultrafast timescales and the segregated carriers are retained in distinct columns [5]. However, strong donor-acceptor character does not guarantee productive catalysis. If the charge-transfer state lies too low in energy, the framework may sacrifice redox driving force, while excessive localization can slow transport to the pore surface. Effective design, therefore, requires a balance among optical absorption, the driving force for charge separation, carrier mobility, and the preserved redox potential.

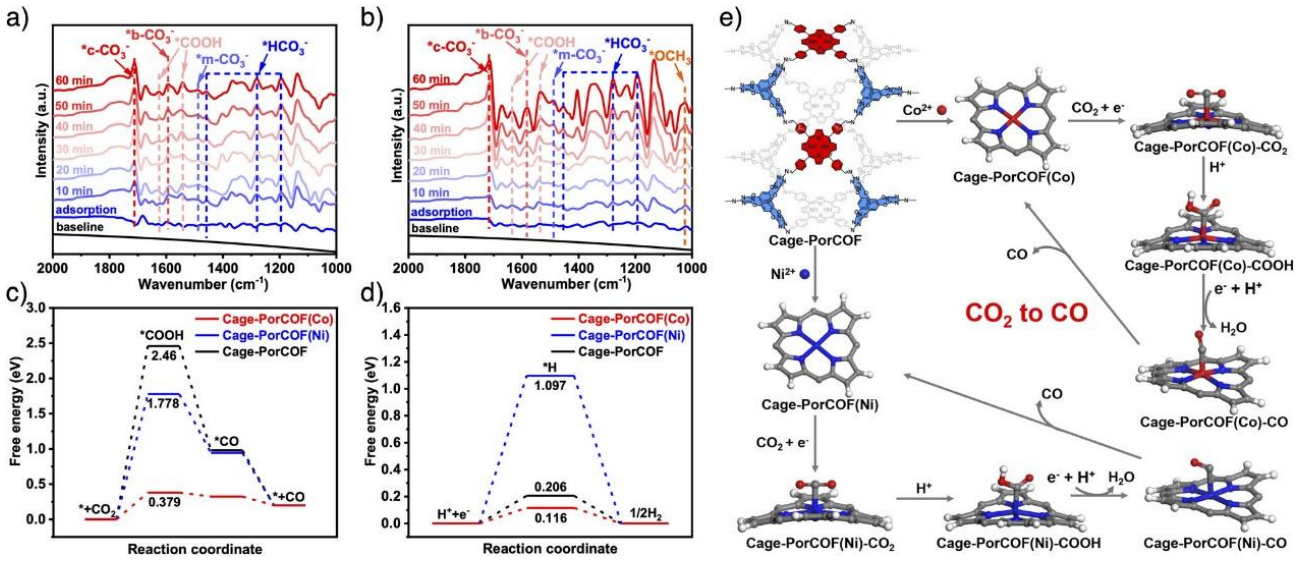
After exciton dissociation, electrons must reach reduction sites while holes are consumed by the coupled oxidation reaction. In metal-free COFs, polarized linkages or heteroaromatic groups can contribute to CO_2 activation; in metalated COFs, isolated metal centers, cooperative pairs, or clusters can accept electrons and bind intermediates. Figure 1 connects these transport and chemical requirements to the stoichiometric constraints above, showing why an energetically accessible reduction pathway can still be limited by carrier delivery or intermediate conversion.

A suitable redox window is the first requirement: the frontier levels in Figure 1A must support both the selected reduction branch and its oxidation partner, but this alignment alone does not establish turnover [23]. The next requirement is site-specific activation. In the Cage-PorCOF comparison underlying Figure 1B, in situ diffuse reflectance infrared Fourier transform spectroscopy (DRIFTS) follows adsorbates under illumination, while density functional theory (DFT) gives a *COOH-formation free-energy change of 0.379 eV for the Co-containing framework, compared with 1.778 eV for its Ni analogue and 2.46 eV for the unmetallated framework [24]. These results connect metal coordination to a plausible chemical bottleneck; the calculated values are reaction free energies, not measured activation barriers. Carrier delivery must also support that chemistry: Figure 1C illustrates how work-function equilibration and selective interfacial recombination in an S-scheme junction can retain strongly reducing electrons and oxidizing holes, a pathway that requires independent validation under illumination [25]. Finally, Figure 1D presents a proposed C-C-coupling and hydrogenation route to ethanol on mixed Cu–Cu(I) ensembles [26]. Operando X-ray measurements and calculations in the source study connect the dynamic copper state with carbonyl-stabilized intermediates. This electrocatalytic example illustrates how local coordination can redirect a C2 pathway; it does not demonstrate ethanol formation on a COF photocatalyst. Together, these constraints motivate the following analysis of exciton dissociation and the later discussion of intermediate-dependent selectivity.

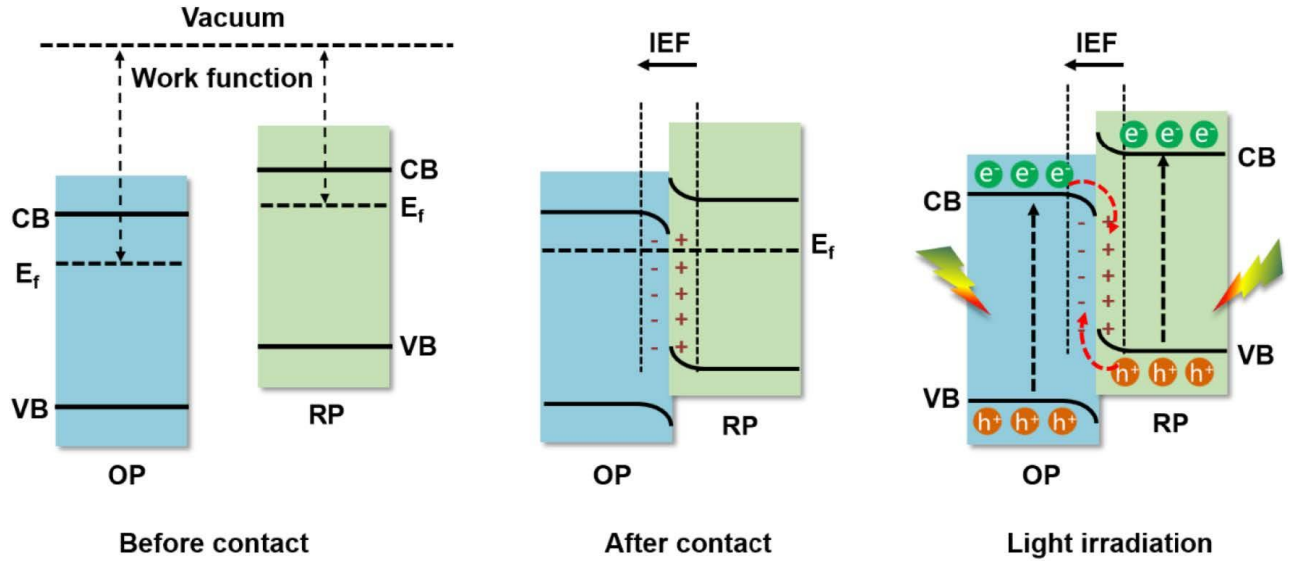
https://doi.org/10.3390/catal16100909



(**A**)

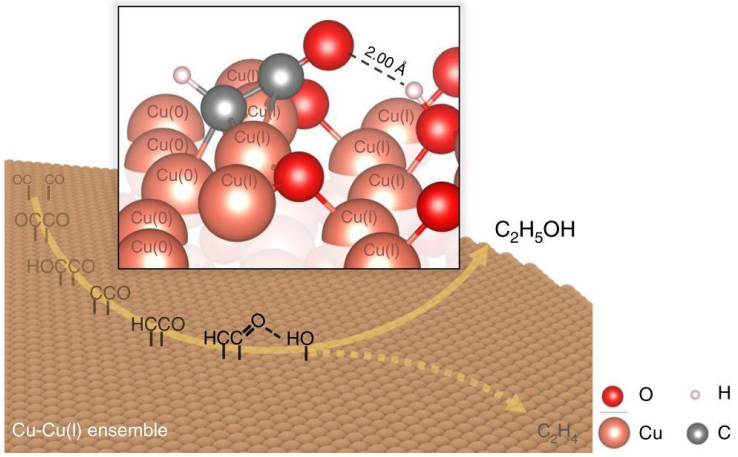


(**B**)



(**C**)

https://doi.org/10.3390/catal16100909



(**D**)

Figure 1. (**A**) Photocatalytic redox window and accessible CO_2-reduction products: (**a**) semiconductor photocatalytic CO_2-reduction system; (**b**) redox potentials and corresponding products [23] (reproduced under CC BY 4.0). (**B**) Cage-PorCOF(Co/Ni): time-dependent in situ DRIFTS for (**a**) Co and (**b**) Ni frameworks; calculated Gibbs free-energy profiles for (**c**) CO formation and (**d**) hydrogen evolution; (**e**) proposed CO_2-photoreduction mechanism [24] (reproduced under CC BY 4.0). (**C**) Work-function equilibration and carrier transfer in an S-scheme junction [25] (reproduced under CC BY 4.0). (**D**) Proposed ethanol-synthesis route and Cu–Cu(I) ensemble in CO_2 electroreduction [26] (reproduced under CC BY 4.0).

2.2. Exciton Dissociation Kinetics and Interfacial Charge Transfer

2.2.1. E_b: The Intrinsic Barrier to Free-Carrier Generation

E_b is the energetic cost of separating the electron and hole from their bound excited state into independently transportable carriers. In an idealized description, E_b reflects the competition between coulomb attraction and dielectric screening, which in real COFs is modified by molecular polarization, finite conjugation length, disorder, and anisotropic electronic coupling. Because thermal energy at room temperature is only about 26 meV, excitons with substantially larger E_b do not dissociate efficiently without an energetic gradient, local electric field, interface, defect-assisted process, or entropy gain. Reported and calculated COF values range from several tens to several hundred millielectronvolts, depending on the framework and method used. Consequently, E_b values should always be accompanied by the measurement or computational protocol, such as temperature-dependent photoluminescence (TDPL), electroabsorption, combined optical/electrochemical gaps, or many-body calculations.

Three structural variables are especially important. First, greater backbone conjugation can delocalize the electron and hole, reduce their effective coulomb interaction, and increase exciton diffusion. π-Bridge engineering has been shown to lower E_b and accelerate photocatalysis [27], while direct computation-guided donor-acceptor design links molecular electronic structure to excitonic behavior [7]. Second, framework planarity and stacking have non-monotonic effects. Better planarity generally increases intralayer delocalization, yet overly strong cofacial stacking can create excimer-like states or deepen traps. Recent work, therefore, explores controlled loss of planarity to reduce interlayer exciton binding [28], as well as decoupled or twisted stacking to enable directional transport without excessive recombination [12,13]. Third, domain size and defect density determine whether an exciton reaches a dissociation site before decaying. Ultrafast studies have revealed large diffusion coefficients in ordered two-dimensional COFs and have shown that mesoscale domain structure alters the observed dynamics [6].

Donor-acceptor architectures provide an additional dissociation force through intramolecular charge transfer and built-in polarization. The donor and acceptor must be selected not only for a narrow optical gap but also for an excited-state offset sufficient to separate charge while retaining reduction and oxidation potentials. Dipole orientation matters: periodic alignment can generate a macroscopic internal field, whereas antiparallel or disordered dipoles may cancel. Linkage orientation, heteroatom substitution, ionic groups, and metal coordination can all tune the electrostatic potential landscape. A rigorous claim of improved dissociation should combine at least one direct or model-based E_b metric with time-resolved evidence showing faster formation or longer persistence of separated charges.

The reported E_b values illustrate why cross-study comparison must remain method-aware: the retained examples include 30.07 meV for Mo/COF, 65.8 meV for TAPT–TT–HQ, and 83.3 meV for TSCOF-2, but these values were obtained from different thermal or optical fitting procedures. The unmetallated parent PY–CN–BIP has a TDPL-derived exciton activation energy (E_a) of 91.6 meV, compared with 138.0 meV for PY–NC–BIP; a directly comparable E_b for PY–CN–BIP–Ni is not reported in the source study. Temperature-dependent photoluminescence can provide an activation-like estimate, yet it depends on emissive-state assignment, fitting range, and the assumption that thermal detrapping is the rate-limiting process. Optical/electrochemical gap differences are experimentally accessible but inherit uncertainties in band-edge and electrochemical-potential assignments. Electroabsorption or Stark spectroscopy probes field-induced changes but may be limited by weak signals and geometry. TDDFT or many-body calculations offer molecular-level interpretation, while their values depend on the functional, dielectric treatment, finite fragment or periodic model, stacking registry, and disorder. E_b should therefore be reported together with temperature, fitting model, dielectric assumptions, domain/stacking model, and uncertainty; a smaller E_b alone is not evidence of higher CO_2-reduction activity.

2.2.2. Interfacial Charge Transfer: Competition with Charge Recombination

Exciton dissociation is necessary but not sufficient. Once free carriers are generated, the electron-transfer rate to the catalytic site must exceed the rates of geminate recombination, bulk trapping, and interfacial back transfer. A useful kinetic picture compares the dissociation rate constant (k_{diss}), recombination rate constant (k_{rec}), transport rate constant (k_{trans}), and interfacial catalytic electron-transfer rate constant ($k_{cat,\,ET}$). Increasing k_{diss} while leaving k_{trans} or k_{cat} unchanged can cause charge accumulation in traps. Conversely, a highly active metal site cannot improve turnover if most excitons decay before electrons reach it. This explains why effective systems often integrate a light-harvesting domain, a directional transport pathway, and a catalytic center in close electronic communication.

Band-orbital alignment, interface dipoles, and built-in electric fields provide a thermodynamic driving force. Type-II heterojunctions can spatially separate electrons and holes but may reduce the redox power of both carriers. S-scheme configurations are intended to retain the strongly reducing and oxidizing carriers while eliminating the weaker pair. However, the proposed pathway must be supported by spectroscopy rather than inferred only from band positions. Early COF-semiconductor heterojunctions, such as COF-5/CoAl-LDH [29] and gas–solid COF/MOF S-scheme systems [30], demonstrated that interfacial construction can enhance charge utilization. More recent COF-only strategies demonstrate that interlayer coupling itself can function as an interface: imine isomerization [11], controlled layer decoupling [12], twisted stacking [13], and Ag-N-Ag interlayer bridges [31] alter the route and timescale of charge migration.

The experimental signatures of productive transfer should be interpreted collectively. Steady-state photoluminescence quenching may indicate charge separation, but it can also arise from nonradiative traps. Time-resolved photoluminescence distinguishes changes in emissive-state lifetime but may not directly track dark charge-separated states. Femtosecond transient absorption can resolve exciton decay, charge-transfer-state formation, and early trapping; nanosecond-to-microsecond measurements determine whether electrons survive long enough for catalytic turnover. Transient surface photovoltage probes directional charge displacement near interfaces, while photocurrent and impedance provide ensemble-level evidence under electrical bias. More reliable assignments combine these techniques with selective quenchers, wavelength-dependent excitation, and operando changes at the active site.

Four carrier stages should be kept separate in mechanistic assignments: exciton generation is photon absorption and formation of a correlated electron–hole pair; exciton dissociation is the creation of spatially or energetically separated carriers; charge separation/transport is their survival and migration through the framework or across an interface; and charge utilization is electron transfer into a chemically competent site followed by intermediate conversion. A material can improve one stage while failing at another—for example, a low E_b can increase the carrier population but still produce low activity if transport, active-site capture, surface PCET, or intermediate desorption is slow.

2.3. Thermodynamic and Kinetic Basis of the Hydrogen Evolution Reaction (HER) Competition

Product selectivity emerges from the free-energy landscape and the flux of electrons and protons through it. Thermodynamic potentials indicate whether a net transformation is possible, but they do not identify the dominant surface pathway. The key quantities are adsorption free energies and activation barriers for competing intermediates. Weak *COOH binding suppresses CO_2 activation; excessively strong *CO binding hinders desorption and can favor deeper reduction or poisoning. Stabilization of *OCHO favors formate, whereas stabilization of *CHO, together with sustained electron and proton delivery, favors methane. C-C coupling requires two carbonaceous intermediates to coexist at suitable separation and orientation, making multinuclear sites and pore confinement particularly relevant. Charge-polarized and asymmetric sites are increasingly recognized as routes to breaking simple adsorption-energy scaling relationships and promoting C_{2+} chemistry [1].

Hydrogen evolution competes for both protons and electrons. Its relative rate depends on water activity, proton donors, surface hydrophilicity, hydrogen-adsorption energy, and the kinetics of CO_2 supply. A hydrophobic or CO_2-philic pore may suppress proton access and enrich the substrate, thereby favoring carbon products even without changing the intrinsic band structure. Conversely, insufficient proton transfer can arrest the CO_2 pathway after one-electron activation. The optimal microenvironment is therefore product-specific: CO-selective sites benefit from rapid *COOH formation and facile *CO release; formate-selective sites require O-bound stabilization and controlled protonation; methane and C_{2+} pathways require longer carrier lifetimes and sustained local electron density. The La-Ni COF, for example, integrates an optically active La-associated domain with a Ni catalytic site to facilitate directional transfer and *COOH formation, achieving high CO selectivity without an external photosensitizer [16]. Descriptor-guided Rh-TMP-COF similarly links the conduction-band minimum and *COOH formation free energy to measured CO production [17]. These systems illustrate how photophysical supply and surface energetics must be optimized together.

This coupled view also defines the standard for mechanistic proof. A claim that a structural modification improves selectivity should ideally demonstrate: a measurable change in exciton dissociation or free-carrier lifetime; faster or more directional transfer to the active site; a change in local electronic structure or adsorption configuration; altered free-energy barriers or intermediate populations; and isotope-validated product formation under controlled conditions. Establishing this chain is the foundation for the structural and electronic engineering strategies discussed in Section 3 and the product-specific mechanisms analyzed in Section 4.

3. Structural and Electronic Engineering of COF Photocatalysts for Exciton and Charge Modulation

The structural programmability of COFs is useful only when a molecular modification leads to a measurable change in the entire photocatalytic sequence. For this reason, the following discussion separates intrinsic backbone regulation from externally introduced interfaces. It evaluates every strategy through the same causal chain: modification of electronic coupling and dielectric screening; changes in E_b or dissociation kinetics; redistribution and transport of free carriers; delivery of electrons to a catalytic site; alteration of intermediate adsorption or activation barriers; and, finally, isotope-validated product formation. This framework avoids equating a red-shifted absorption edge, quenched photoluminescence, or increased photocurrent with catalytic improvement in the absence of evidence that the generated carriers reach a chemically productive state [32].

3.1. Intrinsic π-Conjugation Backbone Engineering

3.1.1. Backbone Extension: Bandgap Narrowing and Charge Delocalization

Extending the π-system is a direct way to increase oscillator strength, broaden visible-light absorption, and reduce the energetic penalty for intraframework carrier motion. In sp^2-carbon-linked COFs, replacing a twisted phenyl connection with an ethynyl-containing building block increased framework planarity and delocalization, improved transient photocurrent and impedance responses. It enabled metal-free gas–solid CO_2 reduction in the presence of water vapor. The ethynyl-bridged BTE-TBD-COF produced CO at 382.0 μmol g^{-1} h^{-1} and showed an AQY of 0.11% at 405 nm, whereas the less conjugated analog was substantially less active [10]. This comparison is mechanistically valuable because the more porous analog adsorbed more CO_2, yet the more conjugated material showed a higher catalytic rate. Charge utilization, rather than equilibrium uptake alone, therefore determined the observed rate.

A homologous core-extension series provides a complementary example. In the benzene-, pyrene-, and anthrathiophene-centered COFs, the anthrathiophene-rich framework combined the broadest electronic delocalization with the longest average photoluminescence lifetime (approximately 1.22 ns compared with approximately 1.03 and 0.97 ns for the less extended analogs) and a CO evolution rate of 301.5 μmol g^{-1} h^{-1}. The result supports a gradient-conjugation design principle in which larger fused units facilitate long-range transport and reduce localized recombination. Nevertheless, the series should not be interpreted as proof that conjugation monotonically lowers E_b because E_b was not directly reported; it is more appropriately treated as evidence that backbone extension can improve the survival and migration of photoexcited states [33]. Similar comparisons of fully conjugated and partially conjugated frameworks have likewise linked continuous π-pathways to improved CO_2 photoreduction. However, their performance remains sensitive to stacking disorder, linkage polarity, and the position of catalytic sites [34].

Backbone modification can also improve catalysis without maximizing formal conjugation. Doebner-type conversion of a framework introduced a nominally nonconjugated structural element while simultaneously modifying photoexcitation dynamics and the electronic environment of the catalytic site. The resulting improvement shows that an extended π-count is not itself the design variable; the relevant quantities are the spatial distribution of the excited electron and hole, the accessibility of a charge-transfer state, and the coupling between that state and the reduction center [35]. Likewise, bipyrimidine-assisted preparation and post-functionalization of vinylene-linked COFs provided a route to combine robust conjugated skeletons with chemically addressable sites for sacrificial-agent-free CO_2 reduction [36]. These studies caution against using optical bandgap narrowing as a surrogate for catalytic quality. Excessive delocalization may increase interlayer trapping or place the excited electron away from the active site, whereas moderate conjugation with favorable orbital alignment can generate a larger productive-carrier population.

3.1.2. Quantitative Modulation of E_b

E_b provides a more physically specific descriptor than the optical gap because it measures the energy required to separate the Coulombically bound electron-hole pair. Two quantitative studies illustrate why the relationship between conjugation and E_b is non-monotonic. In a donor-π-acceptor (D-π-A) series containing phenylene, naphthalene, and anthracene bridges, TDPL gave E_b values of 84.05, 57.42, and 77.32 meV, respectively, compared with 108.79 meV for the unbridged reference. The naphthalene bridge, rather than the most extended anthracene bridge, yielded the lowest E_b because it produced the smallest donor-bridge-acceptor dihedral angle and the most favorable energy-level alignment. It also exhibited the lowest charge-transfer resistance and the highest free-carrier signatures [27]. Thus, increasing aromatic size is beneficial only when it simultaneously improves coplanarity, donor-acceptor coupling, and the route from the charge-transfer state to the catalytic interface.

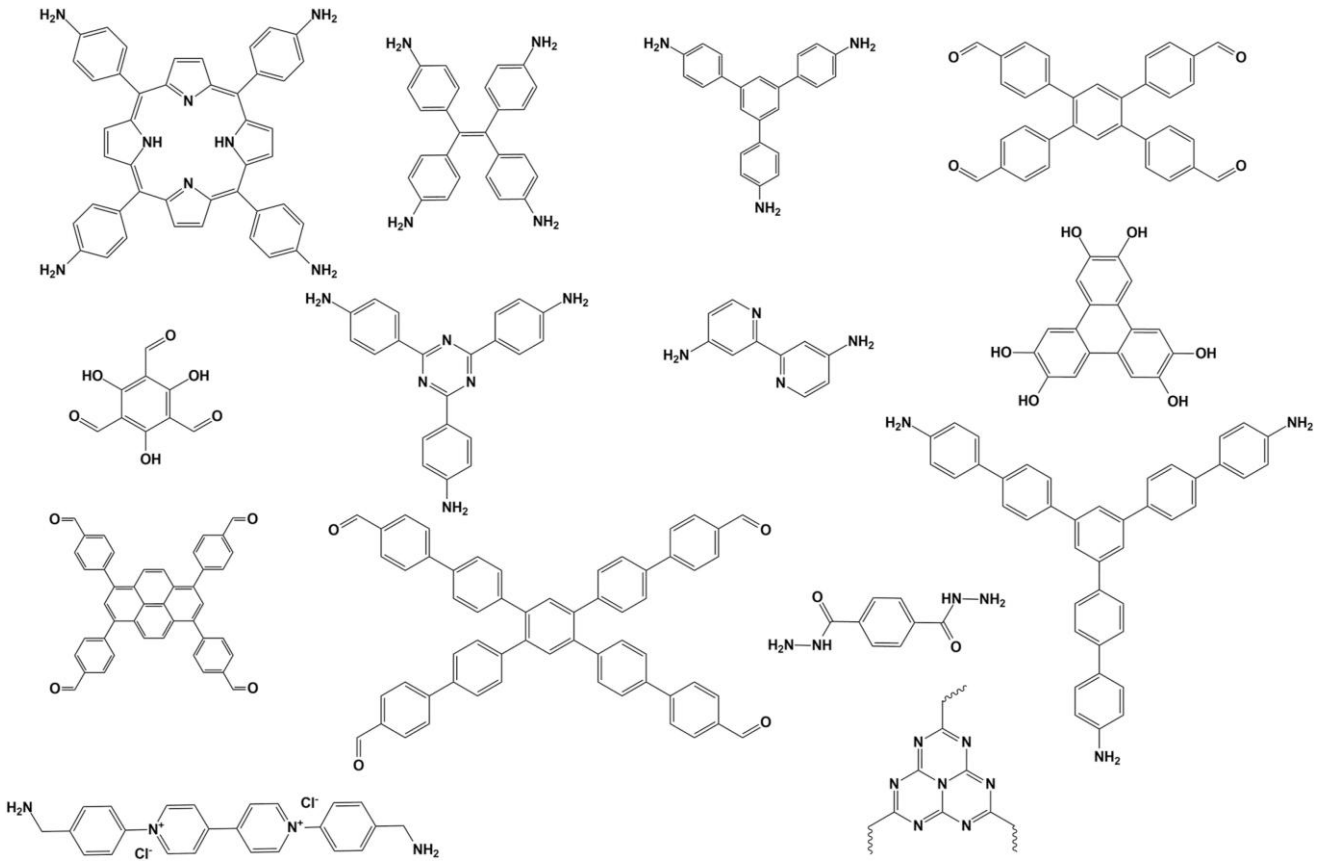
A second quantitative route deliberately reduced the planarity of the local layers. Methoxy substitution increased the torsional angle of a pyrene-derived framework and weakened detrimental interlayer π- π overlap. E_b decreased from 80.4 meV in the most planar hydroxylated COF to 62.5 meV in the unsubstituted material and 43.2 meV in the most distorted methoxy-substituted COF, as determined from TDPL. The lower-E_b material showed faster exciton dissociation and suppressed free-carrier recombination [28]. This result does not imply that crystallinity or intralayer conjugation should be sacrificed indiscriminately. Rather, it distinguishes productive intralayer delocalization from excessive interlayer electronic coupling that can stabilize bound or excimer-like states. An optimal framework can therefore be highly connected within the sheet while electronically decoupled enough between sheets to prevent interlayer recombination.

Computation-guided donor-acceptor screening offers a third route. In time-dependent calculations for a family of donor-acceptor (D-A) molecular pairs, E_b was defined as the difference between the fundamental and optical gaps. Strengthening charge-transfer character reduced the calculated E_b from approximately 0.33 to 0.16 eV across the series, with the methoxy-substituted TAPT pair displaying the largest electron-hole centroid separation and transferred charge [7]. The usefulness of this approach lies in its ability to reject monomer combinations before synthesis; however, calculated gas-phase or cluster E_b values should not be conflated with experimental solid-state values. Dielectric screening, layer registration, defects, guest molecules, and excitation wavelength all reshape excitonic behavior [37]. More robust COF analyses, therefore, combine theory with temperature-dependent spectroscopy, ultrafast transient absorption, and a catalytic comparison under identical conditions.

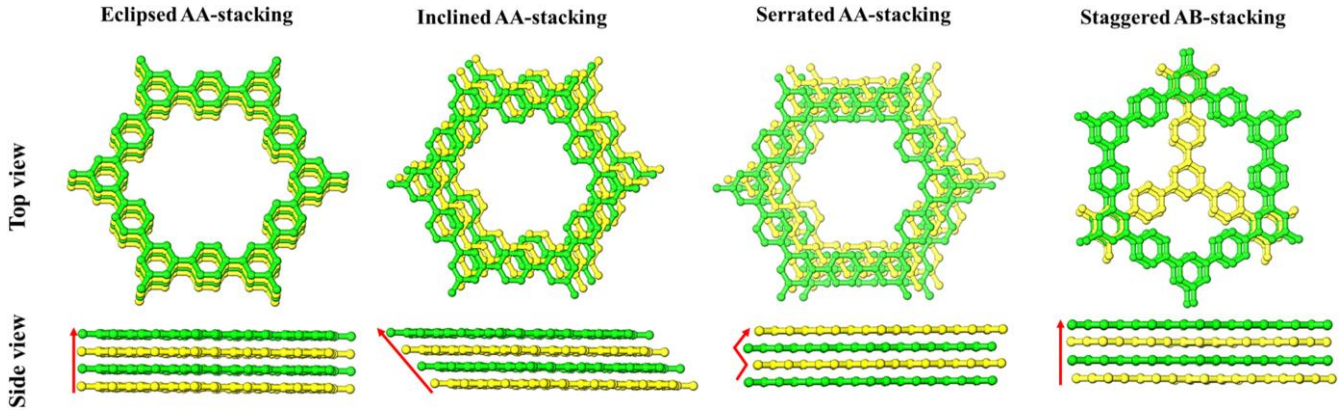
Imine connectivity and framework dimensionality further demonstrate that chemical composition alone is insufficient. Reversing the orientation of an imine linkage switched exciton localization. It altered the charge-separation mechanism, causing one Re-functionalized isomer to support CO_2 to CO photoreduction while the reverse isomer was nearly inactive [11]. Quasi-one-dimensional (Q1D) enaminone-linked COFs similarly combined an intrinsic dipole, broad absorption, and a reduced excitonic penalty; temperature-dependent measurements and transient absorption spectroscopy indicated easier dissociation and more efficient interfacial charge use than in imine- or mixed-linkage analogs [15]. These cases establish a hierarchy of evidence: a calculated or measured decrease in E_b is valuable, but it must be accompanied by evidence that the additional free carriers avoid traps, migrate to the surface, and lower the kinetic cost of the catalytic reaction. These coupled conjugation and exciton-design principles, including quantitative changes in E_b, are summarized in Figure 2.

Figure 2 connects framework geometry with charge-management evidence. The monomers and functional units in Figure 2A define the chemical building blocks, while Figure 2B compares stacking registries that alter orbital overlap [2,38]. Figure 2C shows the temperature-dependent photoluminescence, density-of-states calculations, and light/dark XPS comparison for Mo-coordinated COFs; the reported E_b values are 45.03, 57.87, and 53.22 meV for TpPa-COF-Mo, TpBd-COF-Mo, and TpTa-COF-Mo, respectively; the experiments use an external $Ru(bpy)_3Cl_2$ photosensitizer and TEOA, including Ru-to-Mo electron transfer, so this example does not establish photosensitizer-free COF performance [39]. Figure 2D instead provides a coherent donor–acceptor nanosheet example: CYANO-CON has a lower TDPL-derived E_b than BD-CON (31.2 versus 44.2 meV), and transient absorption identifies slower hole trapping and longer-lived electrons under the source conditions [40]. These measurements support improved exciton dissociation and carrier survival. The catalytic experiment is sacrificial hydrogen evolution with Pt, rather than CO_2 reduction; the figure therefore illustrates transferable charge-management principles without proving a CO_2 product-selectivity benefit or an interlayer-decoupling mechanism.

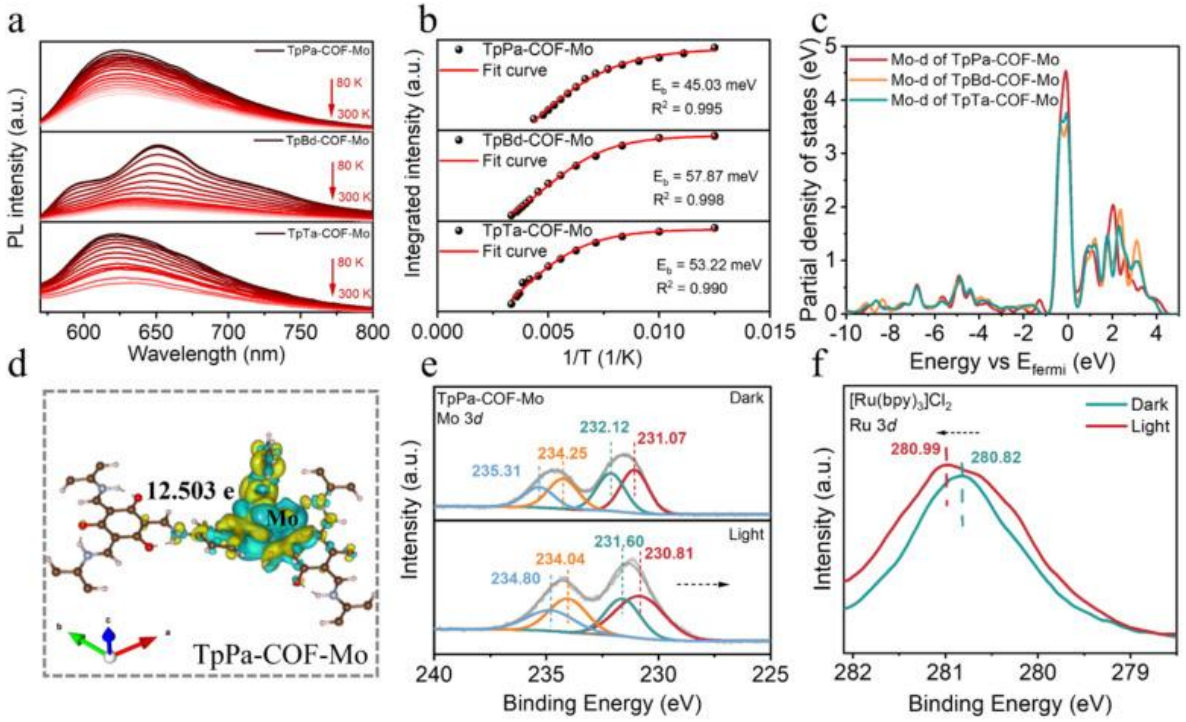
The figures sequence also defines the evidence boundary for E_b-based claims. A lower extracted E_b is mechanistically meaningful only when the measurement or calculation specifies the fitting model, temperature range, dielectric treatment, stacking model, and uncertainty. It should then be connected to a carrier-lifetime or transfer measurement and, ideally, to a catalytic comparison under matched illumination and reaction conditions. Photoluminescence (PL) quenching or stronger photocurrent can support improved charge separation, but neither measurement alone proves that the additional carriers reach CO_2-derived intermediates rather than traps or side reactions.



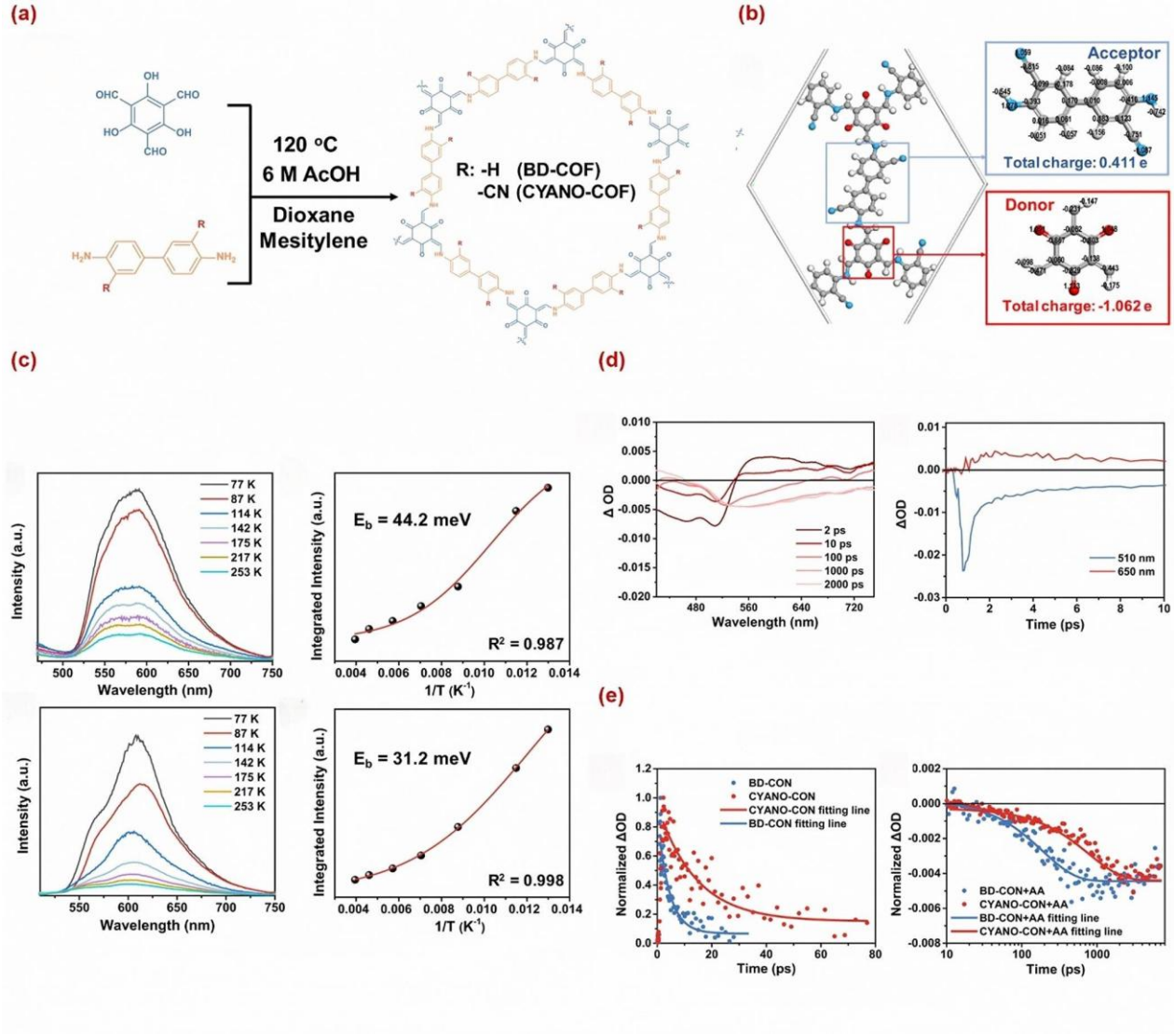
(**A**)


Eclipsed AA-stacking
Inclined AA-stacking
Serrated AA-stacking
Staggered AB-stacking
Top view
Side view

(**B**)



(**C**)



(**D**)

https://doi.org/10.3390/catal16100909

Figure 2. (**A**) Representative monomers and functional units used in COF photocatalysis [38] (reproduced under CC BY 4.0). (**B**) Eclipsed, inclined, serrated, and staggered stacking geometries [2] (reproduced under CC BY 4.0). (**C**) Mo-coordinated COFs with external $Ru(bpy)_3Cl_2$ and TE_{OA}: (**a**) temperature-dependent PL spectra; (**b**) integrated PL intensity and E_b fits; (**c**) Mo d-orbital partial density of states; (**d**) charge-density differences of TpPa-COF-Mo; (**e**) Mo 3d and (**f**) Ru 3d XPS in the dark and under illumination [39] (reproduced under CC BY-NC 3.0; permission required for commercial reuse). (**D**) Donor–acceptor nanosheets: (**a**) synthesis of BD-COF and CYANO-COF; (**b**) calculated donor/acceptor charge distribution; (**c**) temperature-dependent PL and E_b fits for BD-CON and CYANO-CON; (**d**) transient-absorption spectra and kinetics of CYANO-CON; (**e**) hole-trapping and electron-decay kinetics, including ascorbate-assisted electron measurements [40] (reproduced under CC BY 4.0).

3.1.3. Heteroatom and Polar Linkage Modulation: Synergistic Exciton Dissociation and CO_2 Activation

Heteroatoms influence COF photocatalysis through several coupled functions: they change local dielectric screening and dipole moments, provide Lewis-basic CO_2-binding sites, redistribute frontier orbitals, and alter proton-transfer networks. Bromine functionalization is a representative electronic-microenvironment strategy. Rather than serving only as a heavy-atom substituent, bromine changed the charge density around the catalytic domain. It shifted the balance between CO_2 reduction and hydrogen evolution, yielding high CO selectivity [41]. Brominated metal-phthalocyanine COFs similarly illustrate how peripheral substitution can modify the electronic structure of a macrocyclic center while preserving a periodic light-harvesting framework [42]. In both cases, the mechanistic question is whether the substituent increases the steady-state electron density at the reduction site and selectively stabilizes *COOH relative to proton adsorption.

Oxygen-containing linkages and pendant groups serve different functions. Ether-embedded COFs can improve polarity, water organization, and proton delivery without introducing a separate homogeneous mediator [43]. Proton-clamp motifs use cooperative hydrogen bonding to enrich CO_2 and organize proton donors near the pore wall, thereby raising the local substrate concentration while reducing the entropic cost of proton-coupled electron transfer [44]. Multiple heteroatom-hydrogen-bond bridges have also been used to create supramolecular electron-transfer pathways between COF components [45]. These interactions can accelerate transfer, but an overly hydrophilic pore may increase proton access, thereby favoring H_2. Productive heteroatom engineering must therefore balance CO_2 affinity, water activation, and proton availability for the targeted product rather than maximize any one property.

3.2. Donor-Acceptor Architecture for Intramolecular Charge Separation

Periodic donor-acceptor architectures generate an internal electrostatic gradient that promotes intramolecular charge transfer (ICT) and reduces electron-hole overlap. In an ideal D-A COF, photoexcitation redistributes electron density from the donor-rich segment toward an acceptor electronically connected to the catalytic center. This produces three benefits: a lower Coulombic barrier for exciton separation, a directional route for electron migration, and spatial separation of reduction and oxidation equivalents. The earliest ordered bicontinuous D-A COFs demonstrated that periodic donor and acceptor domains can sustain rapid charge separation [5]; current CO_2-reduction systems extend this concept by adding a catalytic site as a third functional element.

Metal COFs containing donor-acceptor-catalytic (D-A-C) sequences explicitly separate these roles. The donor and acceptor create the excited-state driving force, whereas the coordinated metal intercepts the electron and converts CO_2. Reported D-A-C frameworks combine measurable exciton regulation with isotope-validated CO formation, demonstrating that catalytic-site incorporation need not disrupt the light-harvesting pathway [46]. Vinylene-linked donor-π-acceptor metal COFs use a robust, fully conjugated bridge to strengthen ICT and transport [47], while photosensitizing metal COFs have been designed to shorten the distance and time between excited-state formation and metal-site reduction [48]. In each case, the critical experimental signature is not photoluminescence quenching alone, but the formation of a long-lived charge-separated state, together with light-induced changes in the oxidation state or binding energy of the active metal.

Acceptor identity can also determine the depth of reduction. A series of olefin-linked pyrene COFs with systematically varied acceptors shifted the dominant product from CO to CH_4. The cyano-containing CN-COF exhibited favorable charge-transfer dynamics and a CH_4 evolution rate of 34.72 μmol g^{-1} h^{-1} with nearly 100% selectivity. In situ infrared spectra detected the sequence *COOH, *CO, *CHO, *CH_2O, and *CH_3O, while DFT showed that the formation of *CHO was more favorable than CO desorption, explaining the continuation from a two-electron to an eight-electron pathway [49]. This is an important example of D-A architecture controlling selectivity through both photophysics and chemistry: enhanced electron supply sustains sequential hydrogenation, whereas the acceptor-controlled local electronic structure lowers the branch-point barrier.

D-A design nevertheless has trade-offs. Very strong donor-acceptor coupling can localize carriers in deep charge-transfer states, reduce the reduction potential, or accelerate nonradiative decay. Conversely, weak coupling results in a high E_b and a short diffusion length. The optimum is therefore defined by a kinetic window in which exciton dissociation is faster than exciton decay, transport is faster than trapping, and catalytic electron transfer is faster than free-carrier recombination. The design target is not maximal charge separation in an isolated framework but maximal flux of sufficiently reducing electrons into the desired PCET sequence [7,50,51].

3.3. Active-Site and Functional-Group Engineering

3.3.1. Polar Functional Groups: CO_2 Enrichment and Polarization Activation

Polar pore-wall groups increase the probability that a photogenerated electron encounters CO_2 rather than recombining or reducing a proton. Cyano, carboxyl, hydroxyl, ether, and bipyrimidine groups can enhance uptake through quadrupole-dipole interactions and can bend or polarize adsorbed CO_2. Position is as important as composition. Position-dependent carboxyl functionalization produces distinct electrostatic fields and hydrogen-bond geometries, even when the number of carboxyl groups remains unchanged, leading to different adsorption configurations and selectivity [52]. Likewise, chromophore modulation in metal COFs has enabled reduction in low-concentration CO_2 by combining stronger light harvesting with substrate enrichment near the active site [53].

The distinction between bulk uptake and reactive adsorption is essential. A high BET surface area or CO_2 capacity does not guarantee a high turnover rate if most adsorbed molecules are remote from reduction centers. Effective designs collocate enrichment, reduction, and oxidation functions. An integrated framework containing CO_2-enrichment domains and spatially separated redox sites maintained activity under diluted CO_2, demonstrating that pore chemistry can raise the effective substrate activity at the catalytic center [54]. Metalloenzyme-inspired COF membranes similarly use aligned pores and atomically dispersed Fe sites to combine molecular sieving, rapid mass transfer, and well-defined catalytic coordination [55]. The resulting benefit is spatial: shorter diffusion from

an adsorption site to an electron-rich catalytic site reduces the probability that a carrier is lost before PCET begins.

3.3.2. Atomic-Level and Macrocyclic Sites: Intermediate Adsorption Regulation

Single-atom and macrocyclic sites provide a direct route to tuning intermediate adsorption energies. Transition-metal single atoms coordinated by pyridyl, phenanthroline, phthalocyanine, or porphyrin nitrogens exhibit metal-dependent d-orbital occupation and back-donation to CO_2 derived intermediates. A systematic series of transition-metal single atoms in an sp^2-carbon COF showed that changing the metal altered local electronic structure, CO selectivity, and electron consumption, allowing the active center to be selected based on its interaction with *COOH and *CO rather than by metal identity alone [56]. Similarly, Fe-, Co-, and Ni-phthalocyanine COFs reveal that the same macrocyclic framework can produce different reaction rates after changing only the central metal [57].

The first coordination sphere is equally important. Regulating the anions around isolated Co(II) sites modified the electron density and intermediate binding while retaining the same COF backbone [58]. Engineering single Cu sites produced selective CO formation by creating a defined Cu-N environment that activated CO_2 and facilitated *CO desorption [59]. Polarized microenvironments around Ni single atoms extend this principle to the second coordination sphere: pore-wall dipoles alter the charge of the Ni center and reorganize nearby water and CO_2, thereby coupling charge transfer with adsorption selectivity [60]. These studies show why a metal loading value alone is not a useful descriptor; coordination number, ligand identity, axial species, and local field determine the actual catalytic state.

Bimetallic and multinuclear sites can divide elementary steps. In a La-Ni COF, the La-associated environment facilitated light-driven charge management and CO_2 activation, while Ni provided a site for binding carbonaceous intermediates. In situ X-ray absorption and infrared measurements, together with calculations, supported directional electron transfer and a lower barrier for *COOH formation; the material produced CO with high selectivity in the absence of an external homogeneous photosensitizer [16]. One-dimensional (1D) COFs with tunable dual Co sites likewise employ controlled metal-metal separation to modulate cooperative adsorption and electron transfer [61]. For deeper products, distinct sites may be required for *CO generation, C-C coupling, and hydrogenation. Dual modulation of Cu centers and pore topology generated both C_2H_4 and C_3H_6, showing that the geometric arrangement surrounding the metal can be as influential as its oxidation state [62].

A mechanistically complete active-site study should connect operando oxidation-state changes to calculated adsorption energies and observed intermediates. Light-induced XPS or X-ray absorption spectroscopy (XAS) shifts indicate electron accumulation but, by themselves, do not identify the rate-determining step. In situ DRIFTS can show whether *COOH, *OCHO, or *CO populations change, while DFT and Bader analysis quantify how coordination alters charge and free-energy barriers. More robust evidence is obtained when these measurements predict a product switch that is subsequently confirmed by $^{13}CO_2$ labeling.

3.4. Morphology and Heterojunction Engineering

3.4.1. Low-Dimensional Morphology and Interlayer Stacking Modulation

Morphology controls the distance that an exciton or free carrier must travel before reaching an interface. Exfoliated sheets, nanofibers, membranes, spheres, and Q1D chains shorten diffusion paths and expose more active sites, but they also alter dielectric screening and stacking. Dimensional isomerism based on spirobifluorene produced chemically related 2D and 3D COFs with markedly different absorption and charge dynamics. The

2D isomer showed more efficient transient charge behavior and generated CO at approximately 415 μmol g^{-1} h^{-1}, whereas the 3D analog was much less active under identical conditions [14]. Q1D enaminone COFs reduce transverse aggregation while maintaining a continuous polarized chain, thereby facilitating exciton dissociation and charge delivery [15]. 1D phenanthroline COFs bearing isolated Co sites further demonstrate that a short transport direction can be combined with a defined catalytic center [63].

Layer registration is a subtler morphology variable. Perfect eclipsed stacking can improve band dispersion, yet excessive interlayer overlap may create donor-donor interactions, excimers, or traps that compete with intralayer ICT. Decoupling the layers in a Ni-containing COF weakened harmful interlayer coupling, promoted intralayer separation, and yielded a CO evolution rate of 553.3 μmol g^{-1} h^{-1} with 94% selectivity [12]. Twisted stacking provides an alternative: controlled interlayer rotation created directional electron injection toward Ru-bipyridine sites and lowered the measured excitonic penalty, producing both CO and CH_4 under gas–solid conditions [13]. Interlayer Ag-N_2 motifs instead exploited controlled polarization to create a vertical charge-transfer channel; the optimized material reached 20.11 mmol g^{-1} h^{-1} CO with 97.8% selectivity and a 0.058% AQY at 450 nm [31]. These apparently different strategies converge on the same rule: interlayer coupling must be engineered, not simply maximized or minimized.

3.4.2. COF-Based Heterojunctions: Type-II and S-Scheme Architectures

Heterojunctions introduce an external energetic gradient that can separate dissociated carriers after they are generated. Type-II interfaces transfer electrons and holes to lower-energy bands on opposite components, reducing recombination but often sacrificing redox power. S-scheme interfaces retain the most reducing electrons and most oxidizing holes through selective recombination of the weaker carriers. COF-5/CoAl-LDH [29] and TTCOF/NH_2-UiO-66 [30] established that organic–inorganic and COF-MOF contacts can improve gas–solid CO_2 reduction by accelerating interfacial transfer. Later systems used built-in fields in $CuWO_4$/COF [64], imine-bridged ZnO/COF contacts [65], MoO_{3-x}/COF interfaces [66], and covalently assembled COF@g-C_3N_4 [67].

Type-II, S-scheme, and p–n descriptions are not interchangeable labels. Type-II is a band-offset model, the S-scheme is a selective-recombination model that emphasizes the built-in field and preservation of redox power, and p–n is a junction-doping model. In practice, surface photovoltage or Kelvin-probe measurements can establish directional charge displacement, transient absorption can resolve the timescale of interfacial transfer, electron paramagnetic resonance (EPR)/radical trapping can test the retained redox potentials, and in situ vibrational spectroscopy can test whether the transferred carriers actually populate CO_2-reduction intermediates. No single measurement proves a pathway; the assignment should be presented as a convergent evidence chain. Table 1 maps the relevant measurements onto these assignments and their principal limitations.

Table 1. Evidence matrix for assigning charge-transfer pathways in COF heterojunctions.

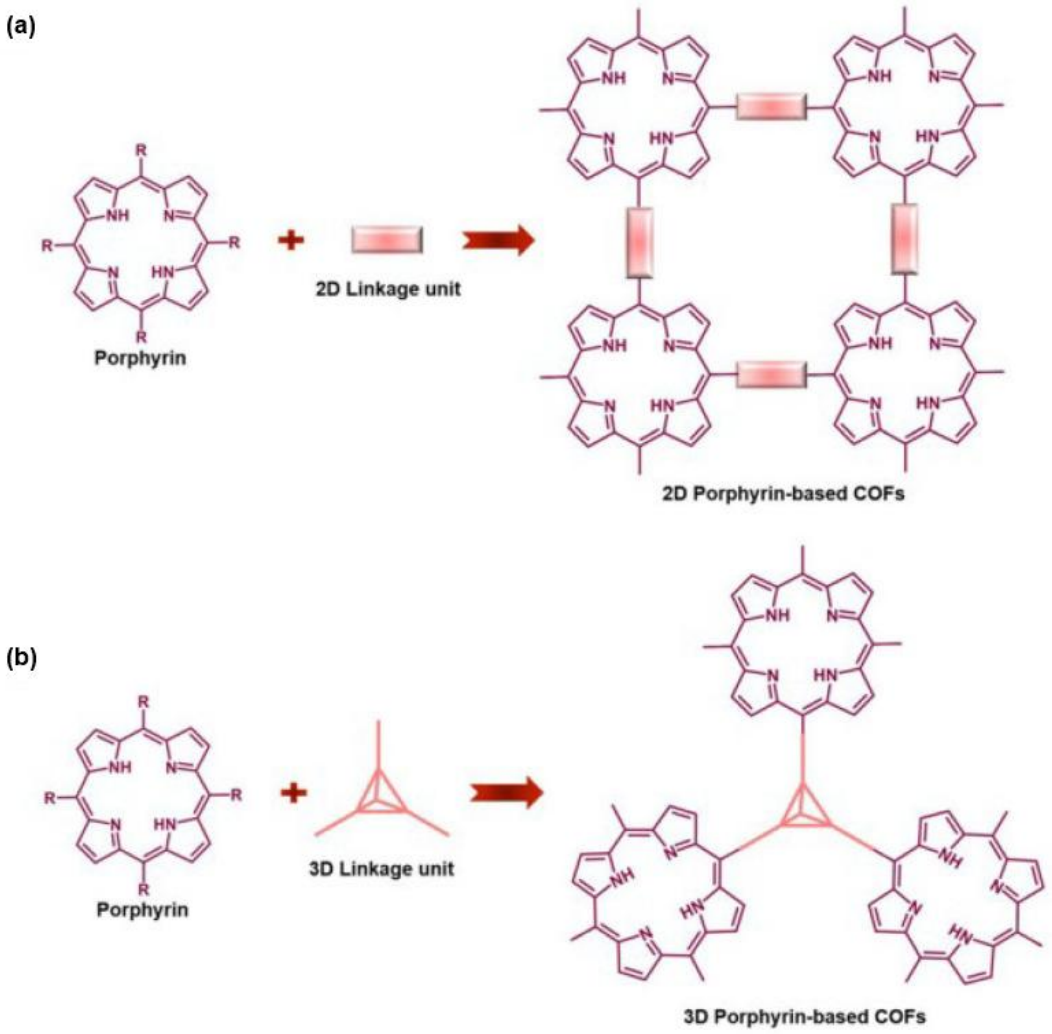
Architecture	Expected Carrier Outcome	Useful Evidence	Interpretive Caution
Type-II	Electrons and holes move to opposite lower-energy bands; spatial separation is favored but redox power can be weakened.	Band positions, selective photocurrent/SPV, transient absorption, and wavelength-dependent carrier mapping.	Band alignment alone cannot establish the direction or productive utilization of the carriers.
S-scheme	The weaker electron–hole pair recombines across the interface, retaining the most	Work-function/KPFM or SPV evidence for an interfacial field, light-induced XPS, transient absorption, EPR	A conventional band diagram or stronger activity is insufficient; multiple orthogonal probes are required.

	reducing electron and most oxidizing hole.	radical trapping, and operando intermediate signatures.	
p–n junction	The depletion region and built-in field bias carrier migration between p- and n-type components.	Carrier-type determination, Mott–Schottky, Kelvin-probe/SPV, photocurrent polarity, and interface-sensitive spectroscopy.	The p/n labels and interface contact must be independently established; charge transfer may coexist with traps or Type-II-like states.

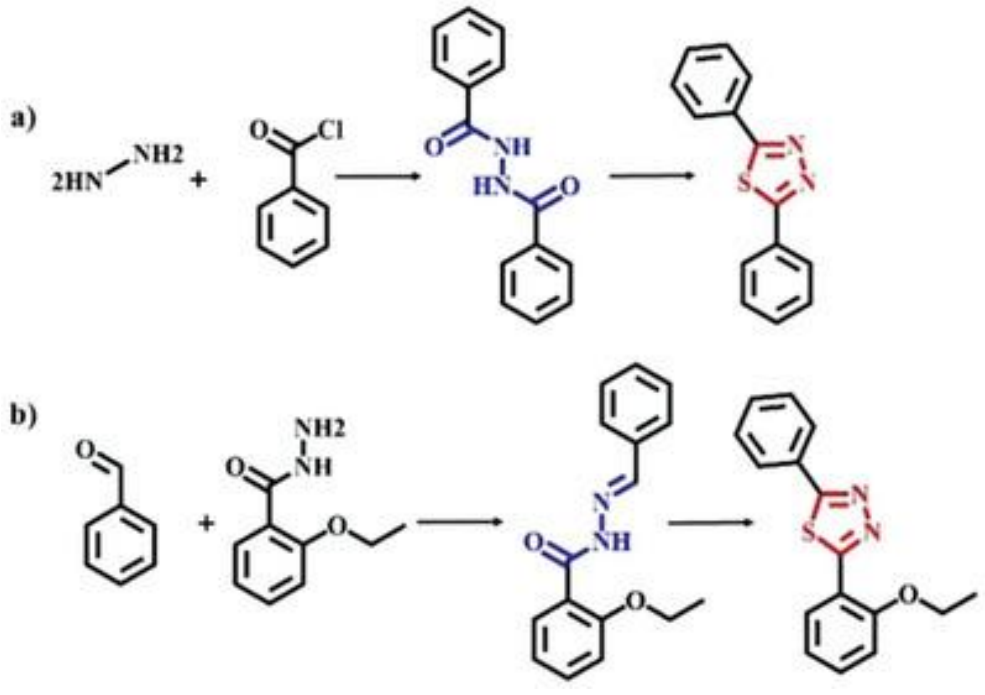
A convincing S-scheme assignment requires more than calculated band positions. It should include work-function or Kelvin-probe evidence for the direction of equilibration, light-induced XPS shifts, radical-trapping or EPR signatures that preserve strong redox carriers, and transient measurements showing faster interfacial transfer. The L-cysteine-bridged $Bi_3TiNbO_{8.5}F$@COF-2CN system is instructive because the molecular bridge provides a defined chemical pathway rather than a weak physical contact. Bi-S coordination and hydrogen bonding strengthened coupling, and the built-in field directed electrons toward the inorganic formate-producing center. The heterojunction generated HCOOH at 314.7 ± 19.4 μmol g^{-1} h^{-1} with 96.0% selectivity while suppressing H_2 [68]. Iron tungstate/COF interfaces similarly unified CO_2 adsorption and reduction domains [69], whereas plasmonic Bi- and MXene-containing hybrids add hot-carrier or local-field effects [70,71].

Heterojunction design must nevertheless preserve the conceptual distinction between exciton dissociation and free-carrier transfer. A built-in field can assist separation at an interface, but a tightly bound exciton generated far from that interface may decay before reaching it. Nanoscale domain size, interfacial area, and exciton diffusion length, therefore, determine whether band alignment is kinetically accessible. Effective heterojunction designs combine low-E_b or rapidly dissociating COF domains, chemically coupled interfaces, short transport distances, and active sites positioned on the electron-accumulating side [22,72]. Representative intrinsic and active-site engineering routes are compared in Figure 3.

Figure 3 summarizes (A) porphyrin framework assembly, (B) linkage conversion, (C) two-dimensional topology, and (D) pore-wall nitrogen variation. The transport constraints above originate partly in how a framework is constructed. Porphyrin assembly in Figure 3A illustrates framework construction [73]. Figure 3C compares triangular, tetragonal, and hexagonal 2D lattices constructed from nodes with different rotational symmetries; the geometrical analysis relates building-block length to pore size and π-column density [74]. This primary study supports topology-controlled pore design, rather than the full design space of multicomponent, 3D, and cage COFs. Linkage conversion in Figure 3B changes the bonding chemistry: conversion from N-acylhydrazone to aromatic thiadiazole modifies the electronic structure and improves chemical robustness in the source study [75]. Its photocatalytic tests concern hydrogen evolution, so the example supports linkage design rather than CO_2 selectivity. Figure 3D compares diffraction patterns and structural models of an azine-COF series with different pore-wall nitrogen contents [76]. These structural data establish a basis for comparing frameworks, but the proposed effects on carrier transport and product branching still require the dynamic and catalytic measurements discussed in Sections 4 and 5.

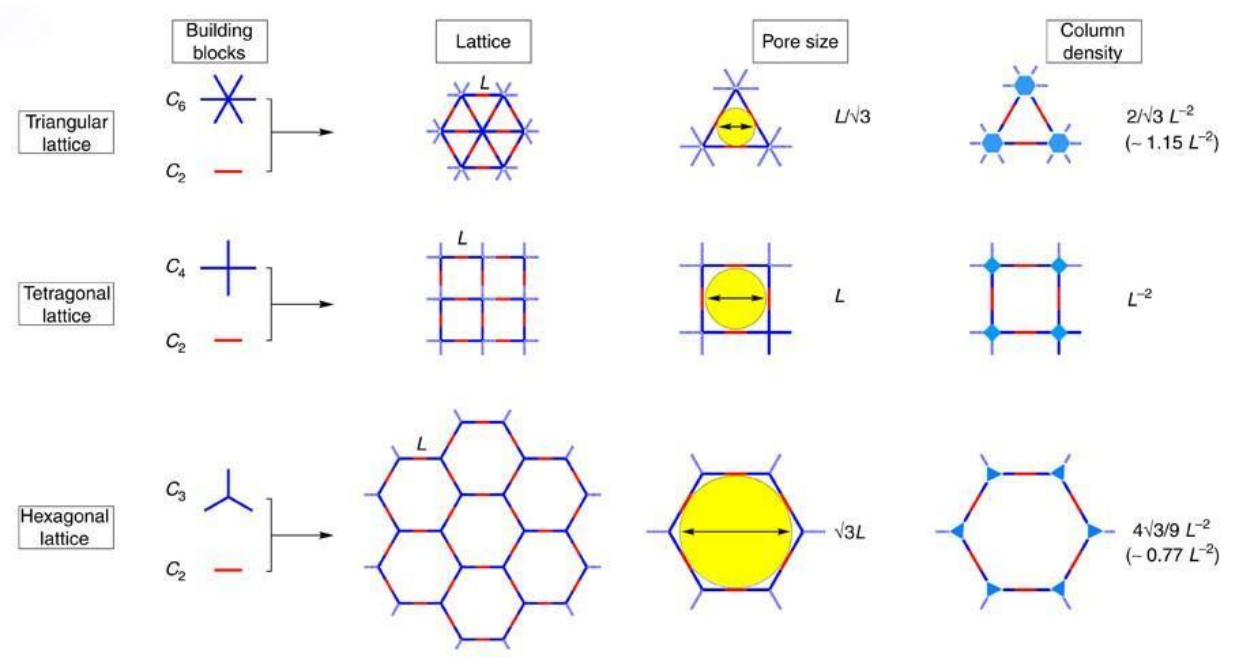


(**A**)

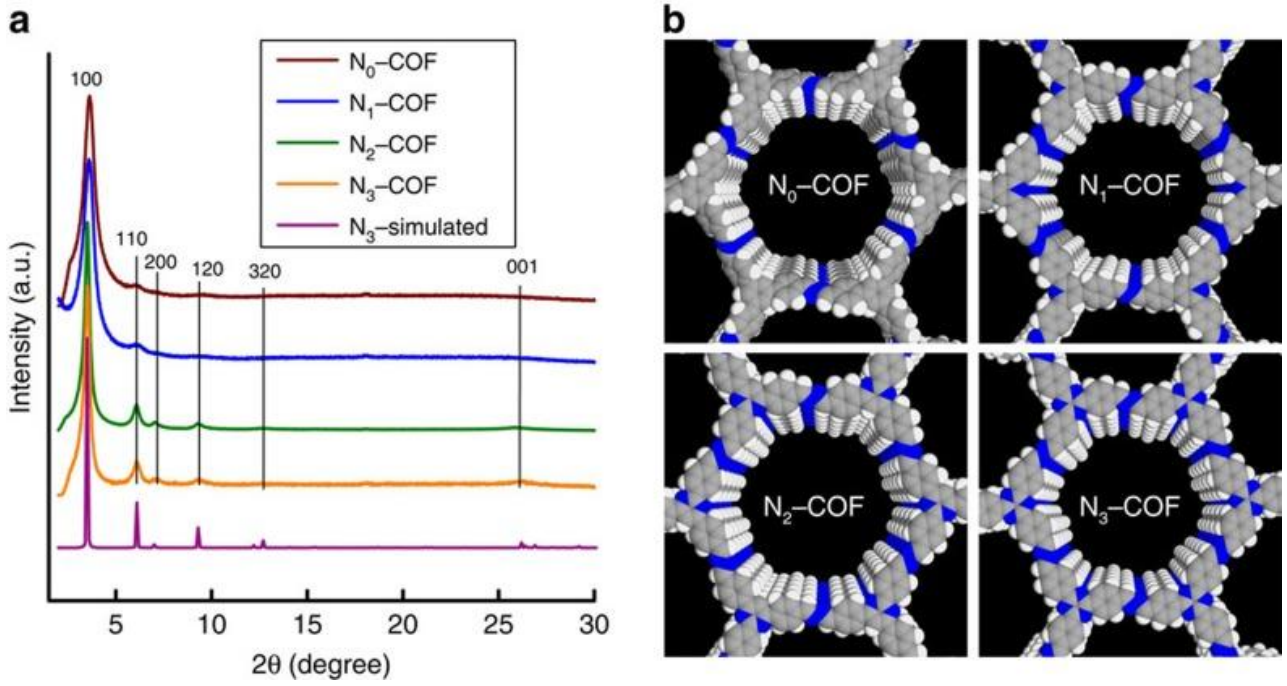


(**B**)

https://doi.org/10.3390/catal16100909



(**C**)



(**D**)

Figure 3. (**A**) Assembly of porphyrin-based (**a**) 2D and (**b**) 3D COFs [73] (reproduced under CC BY-NC 3.0; permission required for commercial reuse). (**B**) Linkage conversion: (**a**) preparation of diacylhydrazine and conversion into thiadiazole; (**b**) model *N*-acylhydrazone reaction followed by thionation, cyclization, and oxidation [75] (reproduced under CC BY 4.0). (**C**) Building-block symmetries, lattice geometries, pore-size relations, and π-column densities for triangular, tetragonal, and hexagonal 2D COFs; adapted from Dalapati et al., Figure 1a [74] (reproduced under CC BY 4.0). (**D**) (**a**) powder X-ray diffraction patterns of N_0-, N_1-, N_2-, and N_3-COFs with a simulated N_3-COF pattern; (**b**) space-filling structural models viewed along the stacking direction, assuming eclipsed stacking [76] (reproduced under CC BY 4.0).

A useful design implication follows from this separation. Synthetic control should be reported at the level of linkage conversion, dimensionality, crystallinity, stacking registry, pore size, and defect density, because these variables change both the local electronic landscape and the transport geometry. The structural figures do not, by themselves, establish a preferred CO_2-reduction product; they define the framework constraints that must later be tested by spectroscopy, computation, and condition-matched catalysis.

4. Product Selectivity Regulation in COF-Based CO_2 Photoreduction

4.1. General Mechanisms Governing Product Selectivity

4.1.1. Thermodynamic Control: Adsorption Energies of Key Intermediates

Product selectivity is determined at branch points where two adsorbed states have comparable free energies. For CO formation, the catalyst must stabilize *COOH sufficiently to activate CO_2 but bind *CO weakly enough to allow desorption. Formate requires preferential O-bound *OCHO stabilization. Methane formation begins when *CO hydrogenation to *CHO becomes more favorable than CO release, while C_2+ products require two carbonaceous intermediates to coexist and couple. These relationships explain why a more negative conduction band does not necessarily produce a more reduced product: band thermodynamics provide the electron, whereas adsorption thermodynamics determine where that electron is used [1].

Descriptor-guided Rh-TMP-COF directly connected the conduction-band minimum and the free energy of *COOH formation with measured CO production. Rh acted as an electron sink and catalytic center, giving a CO rate of 421 ± 56.8 μmol g^{-1} h^{-1} with greater than 99% selectivity in overall CO_2 reduction coupled to water oxidation [17]. In the La-Ni framework, the cooperative metal environment facilitated CO_2 activation and *COOH formation while retaining a pathway for CO desorption [16]. In contrast, fluorination of $Bi_3TiNbO_{8.5}F$ in the cysteine-bridged heterojunction stabilized *OCHO and selected HCOOH [68]. The olefin-linked CN-COF selected methane because the calculated *CHO step was more favorable than CO desorption [49]. These systems illustrate that selectivity can be rationalized only by comparing the free energies of competing branches on the actual light-induced active state.

4.1.2. Kinetic Control: Charge Lifetime and Proton/Electron Flux

Thermodynamically accessible pathways may remain kinetically silent when carrier supply is intermittent. CO and formate are two-electron products, whereas CH_4 requires eight electrons and C_2H_4 requires twelve. Deep reduction, therefore, demands either a charge-separated state that persists across multiple PCET events or a steady electron flux that repeatedly repopulates the catalytic site. Single-atom metal sites with rapid electron trapping can suppress recombination and increase the probability of completing a multistep sequence [56,59]. However, overly strong trapping can also immobilize electrons or lower their reduction potential. The productive lifetime is the time during which an electron remains both chemically accessible and sufficiently energetic.

Proton delivery defines a second kinetic axis. Fast proton transfer is required for *COOH and *OCHO, and for subsequent hydrogenation, but excessive proton activity accelerates hydrogen evolution. Hydrophobic pore segments, cyano groups, and tailored hydrogen-bond networks can limit proton access while retaining enough water to sustain PCET. The cysteine-bridged formate heterojunction simultaneously directed electrons and suppressed H_2, demonstrating that charge routing and proton management can be engineered at the same interface [68]. For methane, the acceptor-tailored CN-COF provided a long enough electron supply and favorable protonation sequence to accumulate *CHO, *CH_2O, and *CH_3O [49]. For ethylene, Pt/Co dual clusters divided C-C coupling

and hydrogenation functions: Pt promoted coupling, whereas Co weakened *CO adsorption and restrained over-hydrogenation to ethane, yielding 7.54 μmol g^{-1} h^{-1} C_2H_4 at 90.1% selectivity [77].

4.1.3. Spatial Control: Pore Confinement and Active-Site Microenvironment

COF pores act as nanoreactors that regulate substrate concentration, intermediate residence time, orientation, and access to proton donors. Confinement is especially important for C-C coupling because two C_1 intermediates must be present at an appropriate distance. Spatially confined Pd nanoclusters in a pyrene COF increased the probability that photogenerated electrons and adsorbed CO_2-derived species encountered the metal cluster before recombination [78]. Atomically dispersed Fe in aligned COF membranes combined through-pore mass transport with site isolation [55]. Proton-clamp traps [44] and position-dependent carboxyl groups [52] further show that second-sphere hydrogen bonding can determine whether CO_2 binds in a C-bound or O-bound geometry.

Pore topology can create cooperative sites without changing the metal itself. Three Cu-containing COFs with similar chemistry but distinct Kagome-type pore geometries exhibited distinct multicarbon activities. The star-shaped topology of BT-COF-Cu facilitated substrate transport and cooperative intermediate coupling, yielding 12.9 μmol g^{-1} h^{-1} C_2H_4 and 0.8 μmol g^{-1} h^{-1} C_3H_6 [62]. Bridge-position isomerism offers another spatial lever. Two COFs containing the same functional elements but different bridge positions displayed markedly different charge distributions and propylene formation, demonstrating that angstrom-scale placement can influence both electron flow and the geometry of carbon-carbon bond formation [79].

4.1.4. Electronic Control: Local Electron Density for Multielectron Transfer

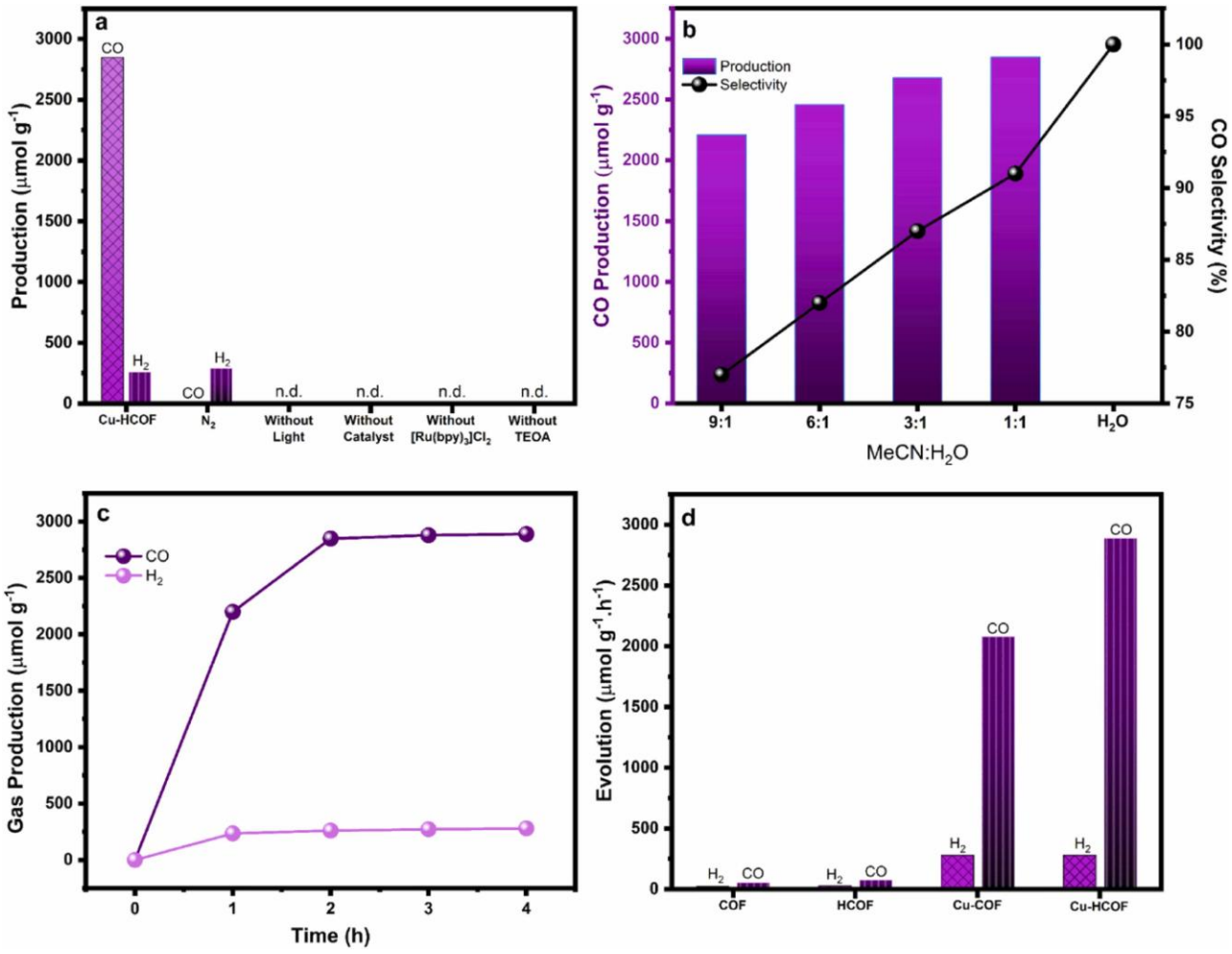
The term local electron density is preferable to a generic claim of charge localization because it can be quantified and directly related to adsorption. Bader charge, differential charge-density maps, operando XPS shifts, and XAS edge changes reveal whether illumination enriches or depletes the active center. A more electron-rich site can back-donate into CO_2-derived orbitals, stabilize high-energy *CHO or *OCCO states, and lower the barrier for multielectron steps. Nevertheless, the optimum is intermediate: excessive *CO binding blocks desorption and can poison the site, whereas insufficient density prevents activation or coupling.

Coordination engineering provides precise control. Changing the metal in single-atom COFs alters d-orbital occupation [56]; changing the axial anions around Co changes the same center without altering the framework [58]; and polarizing the second coordination sphere around Ni tunes the site via an electrostatic field [60]. Charge-polarized or asymmetric pairs are particularly relevant to C_2 formation because unequal sites can bind two carbonaceous intermediates with complementary strengths, breaking the symmetry of equivalent sites that otherwise favors separate C_1 products [80]. The Cu-center/pore-topology system [62] illustrates how adjacent sites can support C–C coupling, whereas dual-Co 1D COFs [61] provide evidence for cooperative CO_2 activation and charge transfer, without independently establishing C–C coupling. Their consequences for intermediate evolution and pathway branching are summarized in Figure 4.

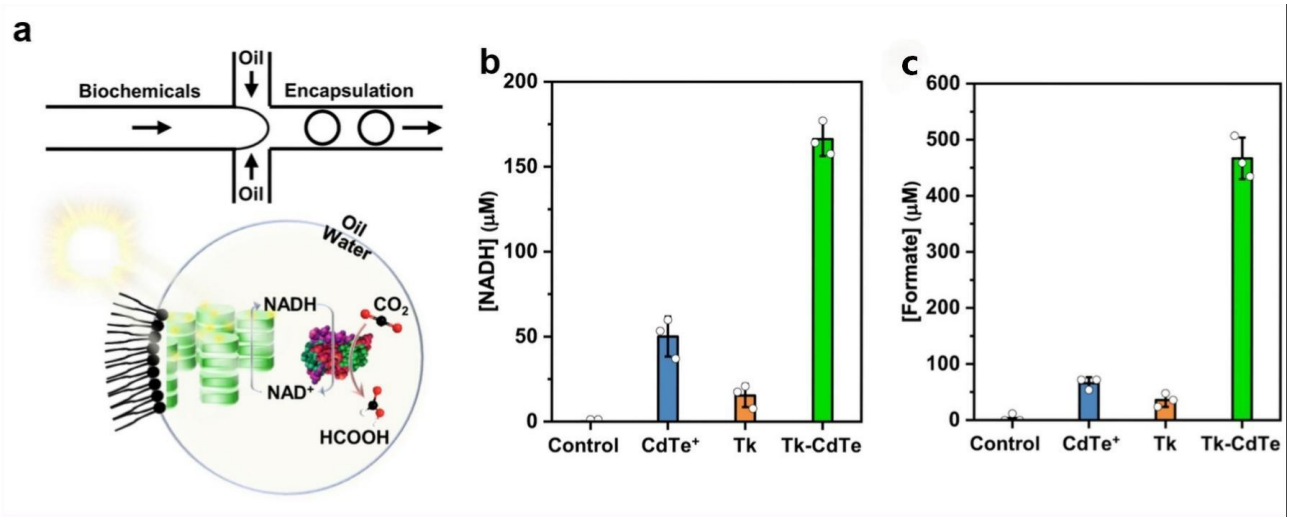
The consequences of site and auxiliary-component design must be assessed through product-resolved controls. In Figure 4A, the Cu-containing hollow COF is compared with metal-free and non-hollow analogues, and the light, catalyst, photosensitizer, and donor controls identify the components needed for CO formation [81]. Because this experiment uses an external Ru photosensitizer, its output cannot be assigned to intrinsic COF light harvesting or included in the strict benchmark below. Figure 4B illustrates an enzyme-coupled pathway in artificial photosynthetic cells: a thylakoid–CdTe hybrid regenerates

reduced nicotinamide adenine dinucleotide (NADH), which supplies CcFDH for CO_2-to-formate conversion [82]. This non-COF example preserves the distinction between carrier generation, cofactor regeneration, and the product-forming enzymatic step; it does not establish COF confinement or a framework-bound *OCHO pathway. Figure 4C compares CO/H_2 syngas evolution across metallosalen COFs, together with component controls, $^{13}CO_2$ tracing, and calculated *COOH energetics [83]. This system uses an external $Ru(bpy)_3Cl_2$ photosensitizer and triethanolamine (TEOA), so its rates belong to the complete sensitized reaction system and are excluded from the strict intrinsic-COF benchmark. Together, these examples show why product selectivity must be interpreted using the complete reaction system, including the origin of reducing equivalents, the catalytic component, and the stated normalization.

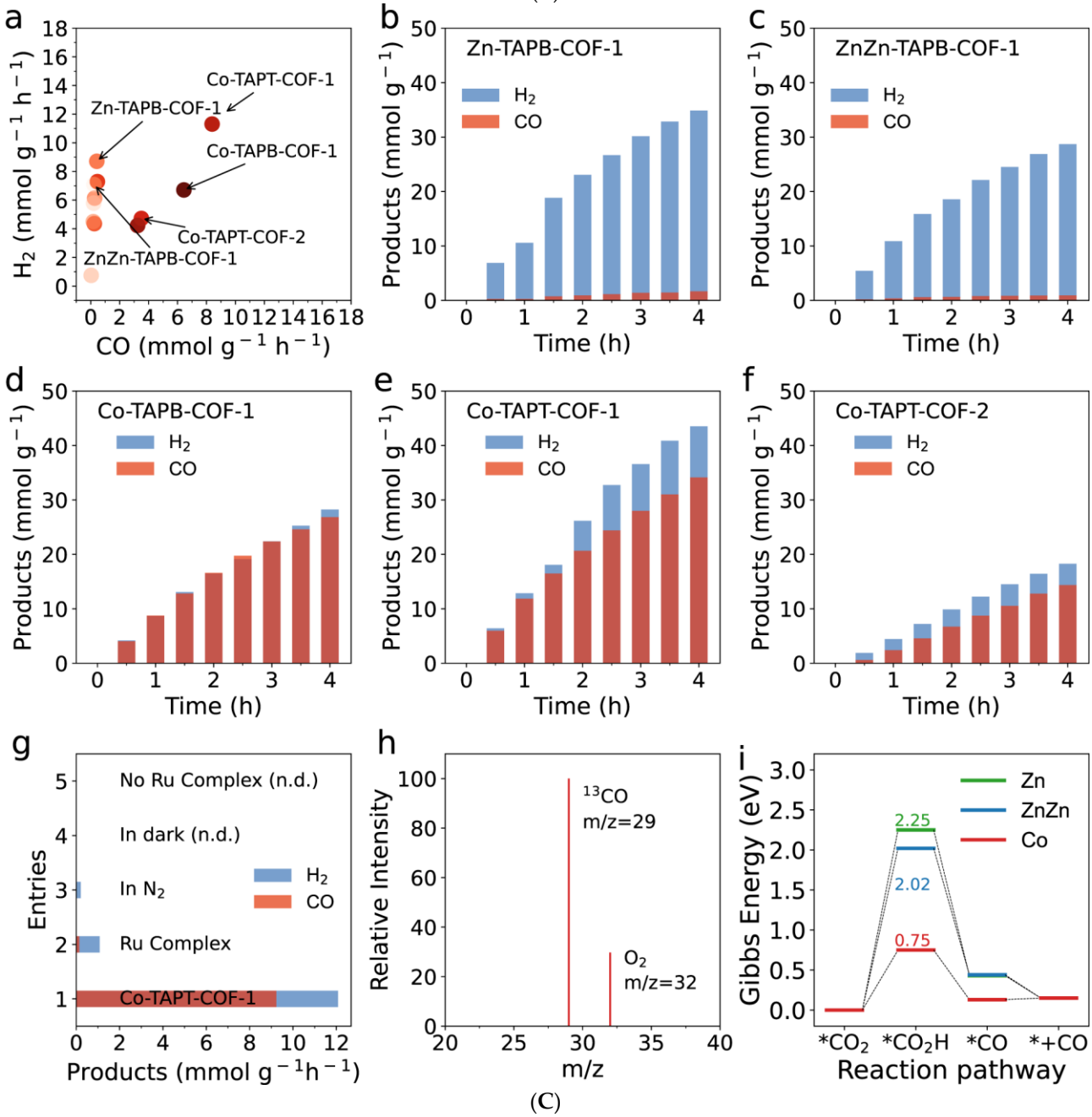
The comparison should be made on three separate denominators. Carbon-product selectivity reports how detected carbon products are partitioned, overall selectivity states whether H_2 and all carbon products are included, and electron-productivity selectivity weights products by their stoichiometric electron demand. Without these definitions, CO selectivity, methane selectivity, and C_{2+} selectivity cannot be compared on a common basis. The figure also illustrates a second boundary: isotope tracing, blank controls, calibrated light input, carbon balance, and post-reaction structural analysis are needed before a product distribution can be treated as a mechanistic consequence of COF design.



(**A**)



(**B**)



(**C**)

https://doi.org/10.3390/catal16100909

Figure 4. (**A**) (**a**) CO/H_2 production under component controls, (**b**) $MeCN/H_2O$ solvent dependence, (**c**) time-dependent gas evolution, and (**d**) catalyst comparison for a Cu-anchored hollow COF with an external Ru photosensitizer [81] (reproduced under CC BY-NC 4.0; permission required for commercial reuse). (**B**) Artificial photosynthetic-cell construction and NADH/FDH coupling (**a**), NADH regeneration after 10 min (**b**), and formate production after 1 h (**c**), comparing the Tk–CdTe hybrid with its components [82] (reproduced under CC BY 4.0). Error bars: mean ± SD, n = 3. (**C**) CO/H_2 rate comparison (**a**), time courses (**b**–**f**), component controls (**g**), 13CO detection (**h**), and calculated CO-formation free-energy profiles (**i**) for metallosalen COFs [83] (reproduced under CC BY 4.0). An external $Ru(bpy)_3Cl_2$ photosensitizer and TEOA are used.

4.2. Selective Formation of C_1 Products

4.2.1. Selective CO Generation

CO is the most frequently reported product because its two-electron pathway is compatible with the carrier lifetimes of many organic semiconductors. High CO selectivity requires a narrow adsorption window: *COOH formation must be accelerated, but *CO must not be stabilized so strongly that hydrogenation continues. Rh-TMP-COF used descriptor-guided metal selection to lower the *COOH barrier and release CO [17]. La-Ni bimetallic sites separated activation and electron-transfer functions [16], and single Cu sites created a defined coordination environment for CO_2 activation and CO desorption [59]. Coordinating-anion regulation around Co provided a further means of tuning the electronic state of an otherwise identical metal center [58].

Metal-free and microenvironmental strategies can reach the same endpoint. Ethynyl extension in BTE-TBD-COF increased the flux of free carriers reaching intrinsic reduction sites, producing 382.0 μmol g^{-1} h^{-1} CO without a metal cocatalyst [10]. Bromine functionalization altered the electronic microenvironment and suppressed competing reactions [41], while control of the carboxyl position changed CO_2 adsorption geometry [52]. These examples indicate that CO selectivity can be improved through either the first coordination sphere or the pore environment, provided the design lowers the *COOH rate-determining step (RDS) without impeding *CO desorption. Hydrophobic domains are additionally useful because they decrease proton adsorption and HER, although complete exclusion of water would prevent PCET.

4.2.2. Selective Formic Acid Formation and Deep Reduction to Methane

Formate selectivity requires a catalyst that favors the O-bound *OCHO over the C-bound *COOH. The L-cysteine-bridged $Bi_3TiNbO_{8.5}F$@COF-2CN heterojunction is a clear example: fluorination adjusted the inorganic center, cyano groups tuned the COF band structure, and the molecular bridge directed electrons to the formate-producing component. DFT showed more favorable *OCHO formation after fluorination, and isotope-resolved nuclear magnetic resonance (NMR)/gas chromatography-mass spectrometry (GC-MS) confirmed the carbon source. The system achieved 314.7 ± 19.4 μmol g^{-1} h^{-1} HCOOH at 96.0% selectivity [68]. Future COF-formate studies should determine whether *OCHO is stabilized by the metal, an adjacent hydrogen-bond donor, or a cooperative pair, as these mechanisms imply different optimization routes.

Methane presents the opposite design requirement: *CO desorption must be suppressed sufficiently for hydrogenation to proceed, while electrons and protons must remain available through six additional reduction equivalents. Acceptor-tailored olefin-linked pyrene COFs showed that product distribution can be switched through organic electronic structure alone. In CN-COF, in situ DRIFTS identified the complete sequence from *COOH to $*CH_3O$, and calculations placed *CHO formation below the competing CO desorption branch, leading to nearly quantitative CH_4 selectivity [49]. Such performance should not be attributed only to a negative conduction band. It results from the

combination of efficient exciton dissociation, sustained electron delivery, an electron-rich reaction center, and a proton-transfer environment that supports stepwise hydrogenation without diverting most carriers to H_2.

4.3. C_{2+} Products: C-C Coupling Mechanisms and Current Limitations

C_{2+} formation is the most demanding selectivity target for COFs. In addition to a twelve-electron requirement for C_2H_4, two carbon-containing intermediates must accumulate, approach one another, and cross a coupling barrier before either desorbs or becomes fully hydrogenated. Charge-polarized active sites can promote this process by binding two intermediates asymmetrically [80,84]. Pore confinement raises their local concentration, while multinuclear centers provide two adsorption positions. The challenge is to combine these properties with a charge-separated lifetime long enough to support slow coupling kinetics.

Three emerging strategies illustrate the design space. First, Pt/Co dual clusters assign Pt to C-C coupling and Co to the regulation of *CO adsorption and hydrogenation, producing C_2H_4 with 90.1% selectivity [77]. Second, a phenazine-based 2D COF increased the fraction of two-carbon products by using an electronically extended backbone that supports prolonged carrier utilization [85]. Third, Cu centers embedded in a star-shaped Kagome pore produced both ethylene and propylene; isotope labeling confirmed the presence of ^{13}C-containing C_1, C_2, and C_3 products, and time-dependent data showed that multicarbon products appeared later than methane, consistent with slower coupling [62].

Bridge-position engineering extends the concept to C_3 chemistry. DA-COF with a favorable bridge arrangement accumulated charge at spatially appropriate sites and generated propylene under visible light in a DA-COF/CuI cocatalytic system, whereas its positional isomer did not [79]. Au25 nanoclusters covalently tethered to a COF provide another example of atomically precise metal ensembles that improve interfacial transfer and lower the *COOH barrier. This Au25/Co-COF example produces CO/H_2 syngas, with reported CO and H_2 rates of 2321.9 and 1717.4 μmol g−1 h−1, respectively; it is not evidence of C_{2+} production [86]. Across these studies, C_{2+} yields remain much lower than the higher CO rates reported for CO-selective systems. The primary bottlenecks are insufficient long-lived electron flux, low coverage of coupling-competent intermediates, competing CO desorption or methane formation, and incomplete control over-hydrogenation after the C-C bond forms.

Future C_{2+} design should therefore combine three quantitative descriptors: the charge difference between adjacent sites, the geometric separation and orientation of those sites, and the residence time of *CO/*CHO under illumination. Microkinetic modeling is needed because a static, low-coupling barrier may not yield C_2 products at low surface coverage. Operando vibrational spectroscopy should track *CO and coupled intermediates, while isotope experiments must exclude carbonaceous residues from COF synthesis. These requirements are especially strict for hydrocarbon products because organic photocatalysts themselves contain abundant carbon [18].

4.4. Performance Benchmarking and General Design Principles

Rate comparisons across the COF literature are easily distorted by different light spectra, irradiance, catalyst mass, reactor geometry, phase configuration, sacrificial donors, cocatalysts, and normalization methods. The benchmark in this review, therefore, includes only studies that report $^{13}CO_2$ tracing and appropriate blank controls, and it separately flags noble metals and external homogeneous photosensitizers. AQY is reported only at the stated wavelength and is not compared with solar-to-hydrogen efficiency. E_b is listed as not reported when no quantitative method is available; qualitative photoluminescence quenching is not converted into an E_b value [18].

Table 2 summarizes the minimum reaction-condition information required to interpret and compare the performance data. Table 3 condenses the full-text screening into a condition-aware benchmark rather than a simple activity ranking. The columns jointly report the framework or composite identity, quantitative excitonic evidence, dominant product, normalized rate, selectivity, wavelength-specific AQY, catalytic auxiliary, and carbon-source validation. This arrangement allows photophysical descriptors to be examined alongside catalytic output, making missing E_b measurements and cocatalyst contributions explicit.

Table 2. Minimum reaction-condition fields required for a fair Table 3 comparison.

Field	Minimum Entry	Why it Changes the Comparison	Status in the Source Literature
Light input	Wavelength/spectrum, irradiance at catalyst, illuminated area, and photon-flux calibration.	Rates and AQY depend on photon energy and incident photon number.	Report as stated; use NR when the source does not provide a calibrated value.
Reaction environment	CO_2 pressure or concentration, gas/liquid/solid phase, reactor volume, flow or batch design, and mixing.	CO_2 solubility and mass transfer can dominate apparent rate, especially in liquid reactors.	Report the exact configuration; do not merge gas–solid and liquid-phase rates without qualification.
Catalyst and reagents	Catalyst loading, particle/film geometry, sacrificial reagent or proton source, cocatalyst/photosensitizer and its loading.	Auxiliary components can supply charge, active sites, or redox equivalents and may dominate activity.	Separate intrinsic COF, composite, and externally sensitized systems.
Time and analysis	Reaction time, product calibration, gas/liquid sampling, isotope controls, blanks, carbon balance, and selectivity denominator.	Early transient production and analytical artefacts can inflate normalized rates or selectivity.	Mark missing fields as NR rather than inferring them from a figure.

Three trends emerge from Table 3. First, quantitative E_b determination remains uncommon: most high-rate systems rely on indirect PL, photocurrent, or band-alignment arguments, leaving the causal link between exciton dissociation and turnover incomplete. Second, higher reported CO rates are often associated with atomically dispersed metals, nanoclusters, interlayer polarization, or heterojunction fields, suggesting that carrier generation must be coupled with rapid electron capture at a chemically competent site. Third, deep-reduction and multicarbon products remain much less common than CO because they require longer-lived reducing equivalents, controlled proton delivery, and cooperative adsorption geometries in addition to favorable band energetics.

Table 3. Excitonic parameters and CO_2-reduction performance of representative COF photocatalysts.

Catalyst	E_b* (meV)	E_b* Measurement Method	Main Product	Yield (μmol g^{-1} h^{-1})	Selectivity (%)	AQY (%)	Cocatalyst/Photosensitizer	$^{13}CO_2$ Labeling	Ref.
Rh-TMP-COF	NR	GW-BSE/DFT descriptor; no experimental E_b	CO	421	>99	NR	Rh single site; no external PS	Yes (GC-MS)	[17]
TF-COF-CONH-Au_{25}-Co	NR	NR	CO/H_2 syngas	CO: 2321.9; H_2: 1717.4	NR	0.58% (400 nm)	Au_{25}/Co sites; no external PS	Yes (MS)	[86]
SBF-2D-COF	NR	NR	CO	415	>99	0.72% (350 nm)	None	Yes ($^{13}CO_2$; $H_2{}^{18}O$)	[14]
Ag0.15-COF	NR	NR	CO	20,110	97.8	0.058% (450 nm)	Ag-N_2 sites; no external PS	Yes (GC-MS)	[31]
BNT-F@COF-2CN	NR	NR	HCOOH	314.7 ± 19.4	96.0	NR	BNT-F heterojunction; no external PS	Yes (NMR/GC-MS)	[68]
MCOF-Ti-Cu	NR	Calculated excitonic analysis; value not extracted	CO	83.48	NR	NR	Cu catalytic site; no external PS	Yes	[46]
En-Q1DCOF	NR	Calculated/temperature-dependent evidence; value NR	CO	126.9 * (24 h average)	≈100	1.94% (450 nm; optimized 20 mg loading)	None	Yes (GC-MS)	[15]
Mo/COF	30.07	TDPL; Arrhenius fit	CO	294.43	98	1.85% (420 nm)	Mo single atom; no external PS	Yes	[56]
TAPT-TT-HQ	65.8	Thermal/exponential fitting + calculation	CO	247 ± 15	95	NR	None	Yes	[35]
TSCOF-2	83.3	TDPL; Arrhenius fit	CO	118.5	NR	NR	None	Yes	[13]
PY-CN-BIP-Ni	NR †	TDPL; thermal activation fit	CO	553.3	94	0.82% (420 nm)	Ni-bipyridine site; no external PS	Yes	[12]
BT-COF-Cu	NR	NR	C_2H_4; C_3H_6	12.9; 0.8	NR	NR	Cu sites; no external PS	Yes	[62]

20% $FeWO_4$/COF	NR	NR	CO	55.9	100	1.1% (450 nm)	$FeWO_4$ S-scheme; no external PS	Yes	[69]
LSPR-TpBpy-Ni	NR	NR	CO	5702	>91	NR	MXene/LSPR+Ni; no external PS	Yes	[71]
MCOF-ANT	NR	NR	$HCOO^-$	1658	≈100	1.59% (450 nm)	Metal-COF active site; no external PS	Yes	[53]
CC-Cu_4SN	NR	NR	CO	29.98	≈99.5	NR	Cu_4 cluster; no external PS	Yes (MS)	[87]
3% Bi/TpBpy-COF	NR	NR	CO	217	99.3	5.1% (500 nm)	Bi nanoparticles; no external PS	Yes	[70]
Pd_3/Py-bTDC	NR	NR	CO	17.75	86.0	NR	Pd_3 nanocluster; no external PS	Yes	[78]
DA-COF	NR	NR	C_3H_6	54.1 *	15.19	NR	CuI cocatalyst; no external PS	Yes	[79]
Co SAS/PAD-COF	NR	NR	CO	3091	93	NR	Co single atom; no external PS	Yes	[63]
TBD-COF-Co-F	NR	NR	CO	504	>98	NR	Co(II)-F site; no external PS	Yes	[58]
[Emim]BF_4@Zn-S-COF	NR	NR	CO	267.95	97.6	2.8% (420 nm)	Ionic liquid/Zn sites; no external PS	Yes	[54]
LaNi-Phen/COF-5	NR	NR	CO	605.8	98.2	NR	La-Ni dual sites; no external PS	Yes (MS)	[16]
BTE-TBD-COF	NR	NR	CO	382.0	NR	0.11% (405 nm)	None	Yes	[10]
COF-5/CoAl-LDH	NR	NR	CO	53.1 *	94.6	NR	CoAl-LDH; no external PS	Yes	[29]

Note: Inclusion required $^{13}CO_2$ validation, at least two independent blank/control tests, a traceable normalized rate, and no external homogeneous photosensitizer. Values follow the source reports. NR, not reported or not directly comparable; * average rate calculated from mass-normalized cumulative yield divided by reaction time: 3045/24 = 126.875 (126.9), 270.54/5 = 54.108 (54.1), and 265.4/5 = 53.08 (53.1) μmol g^{-1} h^{-1} for En-Q1DCOF, DA-COF/CuI, and COF-5/CoAl-LDH, respectively. These interval averages are not initial or steady-state rates. † For PY-CN-BIP-Ni, a directly comparable E_b is not reported; TDPL fitting gives Ea = 91.6 meV for the unmetallated parent PY-CN-BIP (138.0 meV for PY-NC-BIP). For En-Q1DCOF, the standard-loading AQY is 0.66% at 450 nm; 1.94% is obtained at an optimized 20 mg loading. AQY is shown at the reported wavelength; metal sites and heterogeneous cocatalysts are identified.

https://doi.org/10.3390/catal16100909

Selectivity should also be reported in a chemically and electronically transparent manner. Carbon-product selectivity based only on detected carbon products can appear high even when most photogenerated electrons produce H_2. Electron selectivity, calculated from the stoichiometric electron demand of every product, is more informative for comparing CO, CH_4, and C_{2+} pathways. Carbon balance and time-resolved product formation are equally important: early CO formation followed by delayed CH_4 or C_2H_4 indicates sequential conversion, whereas simultaneous formation may reflect parallel sites. For liquid products, independent quantification by ion chromatography, NMR, or calibrated colorimetric methods is desirable, and isotope-resolved NMR is particularly important for HCOOH, methanol, ethanol, and other products that can arise from residual solvents or organic framework degradation.

Three selectivity quantities should be reported separately. Carbon-product selectivity is the fraction of detected carbon products assigned to a target carbon product; overall product selectivity should state whether H_2 and all carbon products are included in the denominator; and electron-productivity selectivity weights each product by its stoichiometric electron demand, allowing CO, formate, CH_4, and C_{2+} products to be compared on a common electron basis. The phrase "selectivity toward carbon products" should therefore be accompanied by the denominator, product list, carbon balance, and H_2 rate.

The benchmark must also separate intrinsic COFs from systems whose apparent performance is dominated by a noble-metal cluster, a molecular metal complex, or an external homogeneous photosensitizer. These systems remain mechanistically valuable because they reveal how a COF transports charge or organizes catalytic sites, but they should not be directly compared with metal-free frameworks. Gas–solid and liquid-phase reactors also address different limitations: gas–solid operation minimizes solubility and mass-transfer constraints associated with dissolved CO_2, whereas liquid systems provide controllable proton donors and facilitate coupling between oxidation and reduction half-reactions. A fair comparison, therefore, requires a matrix of conditions rather than a single rate column. AQY measured at a monochromatic wavelength is the preferred light-utilization metric, but its electron-counting equation must include all products and the incident photon flux at the catalyst. Reporting only an action-spectrum-like trend without calibrated irradiance is insufficient.

A reproducibility matrix should report applied irradiance, CO_2 pressure, catalyst loading, reaction time, reactor design, sacrificial reagent, and spectral bandwidth alongside the normalized rate. Each can change the apparent activity. Where the source does not report a condition, NR is preferable to back-calculation or inference; incomplete reporting limits comparisons even when carbon-source controls are available.

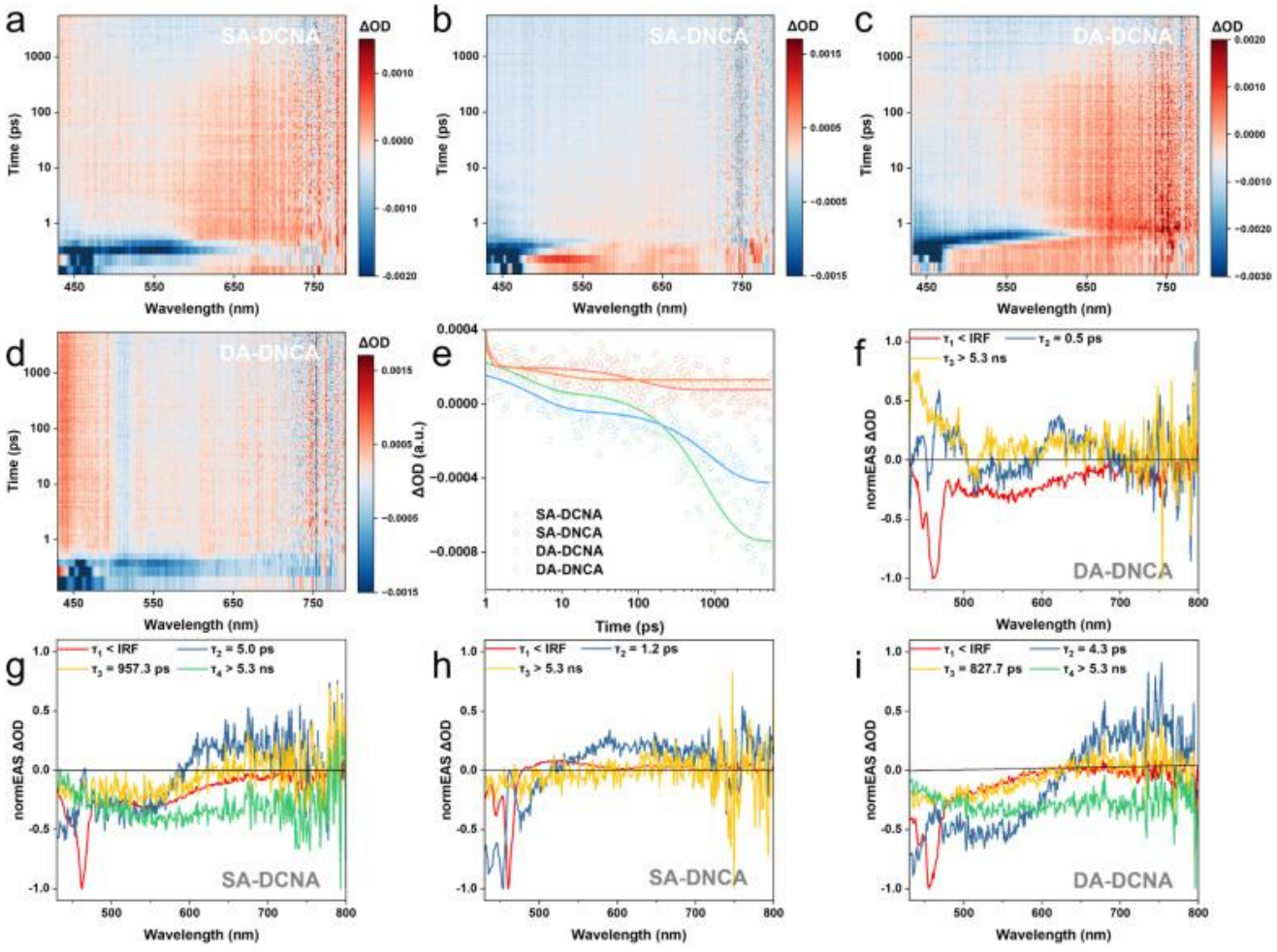
Several general rules emerge. First, optical absorption should be optimized together with E_b and exciton diffusion; a narrow gap is insufficient when excitons remain bound. Second, intralayer delocalization and interlayer coupling must be treated separately, because strong stacking can either enhance transport or create recombination channels. Third, a charge-separation strategy must terminate at a chemically defined site whose local electron density and coordination stabilize the desired intermediate. Fourth, pore microenvironments should be product-specific: CO favors rapid *COOH formation and *CO release; formate requires *OCHO stabilization; methane requires sustained PCET through *CHO; and C_{2+} products require asymmetric multinuclear sites and confinement. Finally, performance claims should be accepted only when isotope tracing, blank controls, calibrated light input, and transparent normalization demonstrate that the measured carbon product is genuine and reproducible. The spectroscopy, theory, and isotope controls required to validate this multiscale structure-activity relationship are consolidated in Figure 5. Table 4 summarizes the relationships among structural design, mechanistic function, and product selectivity in COF photocatalysis.

Table 4. Structure–mechanism strategies for product-selective CO_2 photoreduction over COFs.

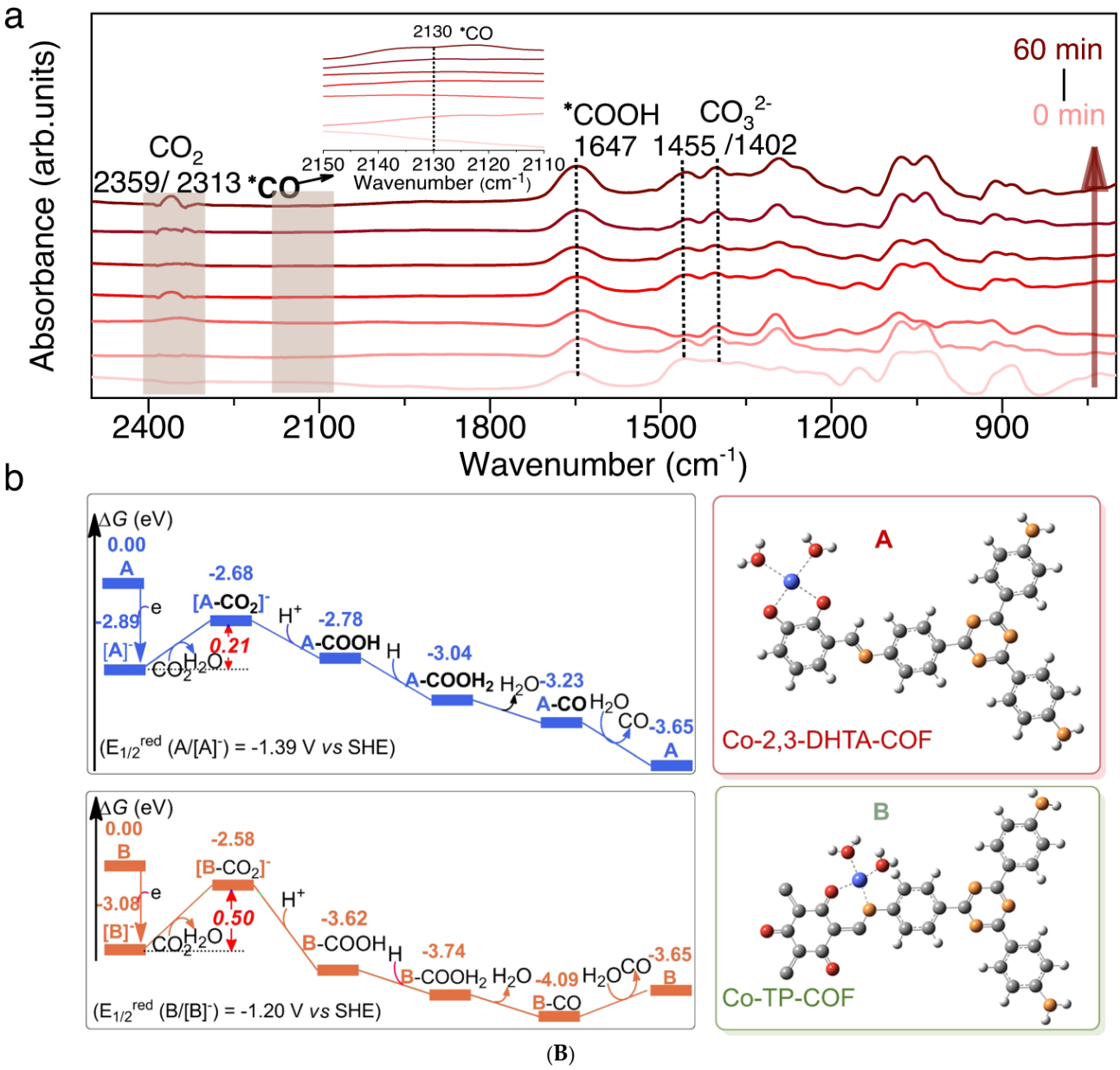
Design Lever	Preferred Outcome	Mechanistic Variable	Main Limitation
Polar or ionic pore walls	CO_2 enrichment and CO/formate selectivity	Adsorption orientation, local electric field, proton accessibility, and suppression of competing H_2 evolution.	Excessive hydrophilicity or overly strong binding can impede mass transfer or product release.
Single-atom or coordinated metal sites	CO, formate, or deeper C_1 products	Metal oxidation state, coordination anion, electron density, and stabilization of *COOH, *OCHO, or *CHO.	The metal can dominate the apparent activity; COF contribution must be separated with matched controls.
Donor–acceptor and linkage engineering	Higher carrier utilization and controlled branch selection	Excited-state offset, dipole orientation, E_b, exciton diffusion, and charge-transfer lifetime.	A narrower optical gap or stronger PL quenching does not by itself prove productive catalysis.
Heterojunction or built-in-field design	Suppressed recombination and retained redox power	Interfacial field, transfer direction, and carrier lifetime at the catalytic component.	Type-II/S-scheme/p–n assignments are easily overinterpreted without orthogonal evidence.
Pore confinement and multinuclear sites	C_{2+} products or sequential CO conversion	Intermediate proximity, *CO coverage, C–C coupling geometry, and local proton/electron flux.	Trace C_{2+} products require isotope, carbon-balance, and time-resolved validation.

Figure 5 presents (A) transient-absorption spectroscopy, (B) in situ infrared spectra and reaction energetics, (C) operando Cu X-ray spectroscopy, (D) electronic-structure and modelling examples, and (E) operando Pt-site analysis. The mechanisms proposed above require complementary measurements because carrier generation, intermediate conversion, and active-site restructuring are different observables. Figure 5A illustrates transient-absorption maps and kinetics in a COF study of organic transformation and H_2O_2 photosynthesis [88]; it is a methodological example rather than direct CO_2-reduction evidence. Figure 5B combines time-dependent in situ ATR-FTIR spectra with calculated CO_2-to-CO pathways at Co-O_4 sites in Co-2,3-DHTA-COF [89]. The *COOH/*CO assignments and calculated ligand-exchange free energies link coordination to a plausible catalytic bottleneck, but the computed ΔG values (0.21 versus 0.50 eV for the comparison catalyst) are not measured activation barriers. Figure 5C shows potential-dependent Cu K-edge XANES and EXAFS during CO_2 electroreduction [26], while Figure 5E presents Pt-site measurements during electrocatalytic hydrogen evolution [90,91]. These non-COF X-ray studies show why the working site can differ from the as-prepared material. Figure 5D combines electronic-structure/optical analysis [92] and infrared-informed machine-learning examples [93] with vacancy-formation and CO_2-adsorption charge-density models for ferroelectric Bi_3TiNbO_9 [94]. These methodological analogues require direct validation before transfer to COF photocatalysts.

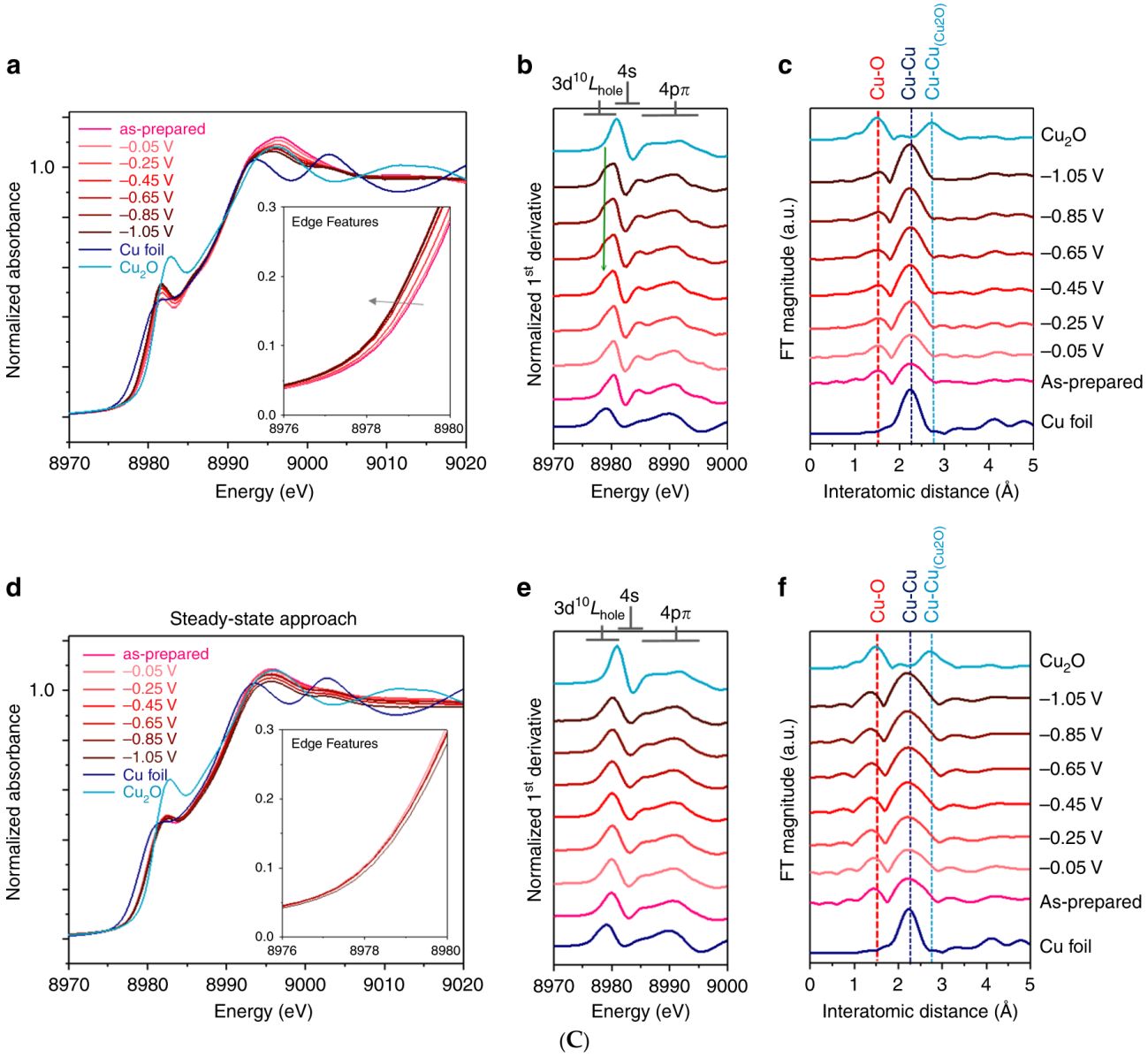
The most defensible mechanistic assignments therefore follow an evidence ladder: carrier dynamics establish when charge is available; operando spectroscopy establishes which site and intermediate are present; theory tests whether the proposed pathway is energetically plausible; and product analysis tests whether the pathway closes with the claimed selectivity. Agreement across these layers is stronger than any single proxy, but disagreement is also informative. For example, a long-lived excited state without an intermediate signal points to inefficient surface utilization, whereas a strong intermediate signal without a persistent charge population may indicate dark adsorption or a transient, non-productive branch.



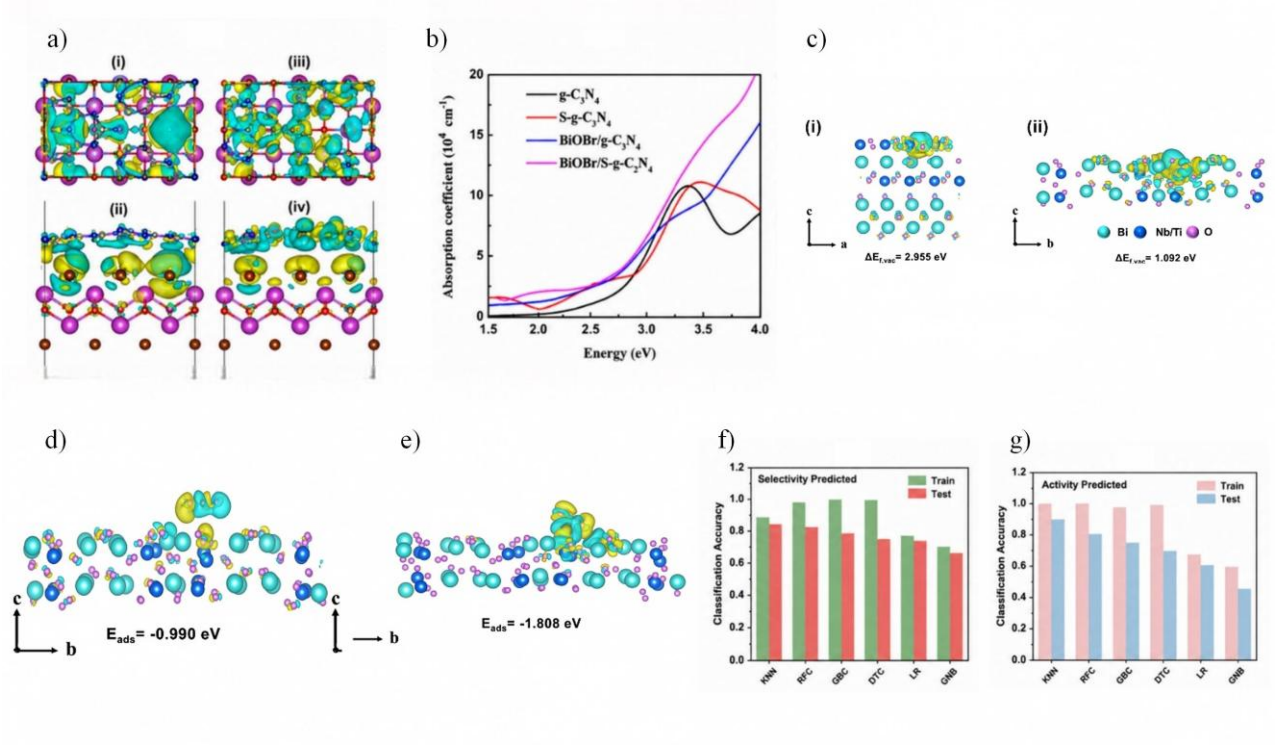
(**A**)


a
Absorbance (arb.units)
2130 *CO
2150 2140 2130 2120 2110
Wavenumber (cm-1)
60 min
0 min
CO2
2359/ 2313 *CO
*COOH
1647
CO3 2-
1455 /1402
2400
2100
1800
1500
1200
900
Wavenumber (cm-1)
b
ΔG (eV)
0.00
A
-2.89
e
[A]-
-2.68
[A-CO2]-
0.21
H+
-2.78
A-COOH
H
-3.04
A-COOH2
H2O
-3.23
A-CO
H2O
CO
-3.65
A
(E1/2red (A/[A]-) = -1.39 V vs SHE)
A
Co-2,3-DHTA-COF
ΔG (eV)
0.00
B
-3.08
e
[B]-
-2.58
[B-CO2]-
0.50
H+
-3.62
B-COOH
H
-3.74
B-COOH2
H2O
-4.09
B-CO
H2O
CO
-3.65
B
(E1/2red (B/[B]-) = -1.20 V vs SHE)
B
Co-TP-COF

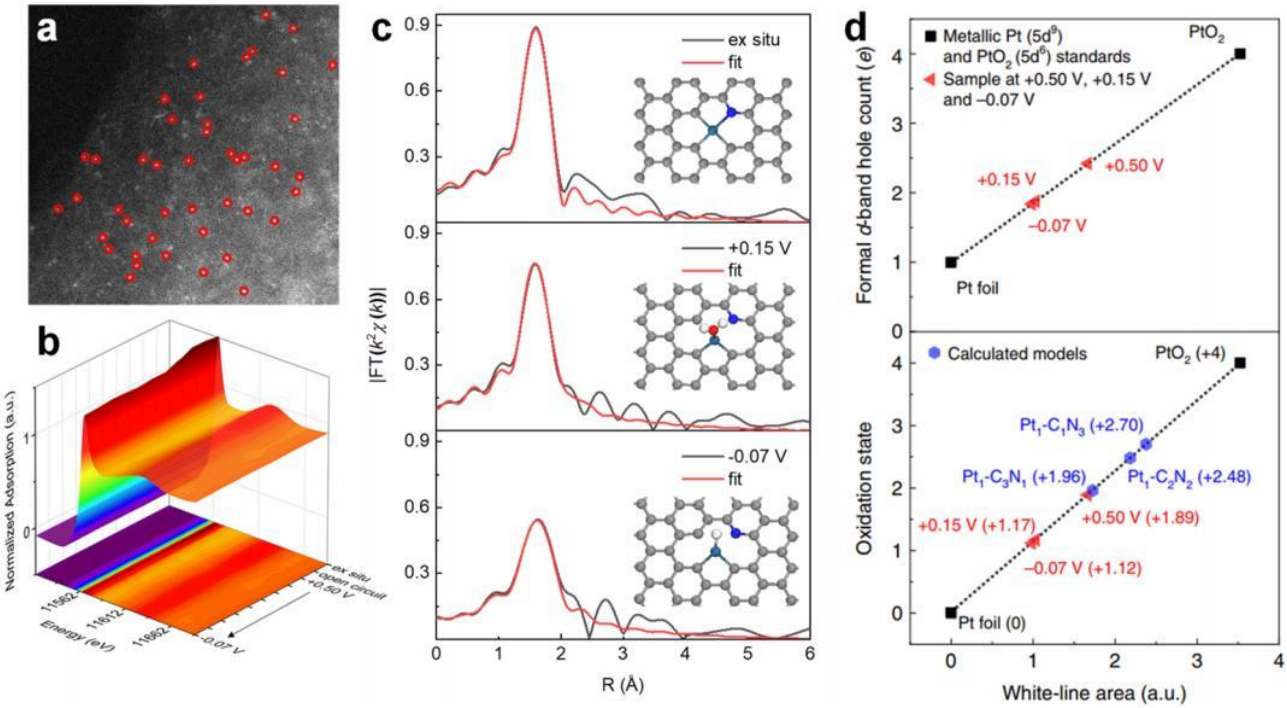
(**B**)


a
b
c
d
e
f
Normalized absorbance
Energy (eV)
as-prepared
−0.05 V
−0.25 V
−0.45 V
−0.65 V
−0.85 V
−1.05 V
Cu foil
Cu2O
Edge Features
Steady-state approach
3d10Lhole
4s
4pπ
Normalized 1st derivative
Cu-O
Cu-Cu
Cu-Cu(Cu2O)
FT magnitude (a.u.)
Interatomic distance (Å)

(C)



(**D**)



(**E**)

Figure 5. (**A**) Transient-absorption analysis for imine-orientation-controlled COFs in organic transformation/H_2O_2 photosynthesis: (**a**–**d**) maps for SA-DCNA, SA-DNCA, DA-DCNA, and DA-DNCA, respectively; (**e**) time–absorption profiles and fits; evolution-associated spectra for (**f**) DA-DNCA, (**g**) SA-DCNA, (**h**) SA-DNCA, and (**i**) DA-DCNA [88] (reproduced under CC BY-NC 3.0; permission required for commercial reuse). (**B**) In situ ATR-FTIR spectra during CO_2 photoreduction (**a**), calculated CO-formation pathways and coordination models (**b**) for Co-2,3-DHTA-COF and Co-TP-COF [89] (reproduced under CC BY 4.0). (**C**) Cu K-edge XANES, derivatives, and EXAFS under a redox-shuttle protocol (**a**–**c**) and steady-state reduction (**d**–**f**) in CO_2 electroreduction [26] (reproduced under CC BY 4.0). (**D**) Electronic-structure and optical-response examples (**a**,**b**) [92] (reproduced under

CC BY 4.0); oxygen-vacancy formation perpendicular/parallel to ferroelectric polarization (**c**), and CO_2-adsorption charge-density differences without (**d**) and with (**e**) a vacancy in Bi_3TiNbO_9 [94] (reproduced under CC BY 4.0); infrared-informed machine-learning selectivity/activity predictions (**f**,**g**) [93] (reproduced under CC BY-NC 4.0; permission required for commercial reuse). (**E**) Electrocatalytic hydrogen evolution: (**a**) single-atom Pt microscopy, (**b**) operando Pt L3-edge XANES, (**c**) EXAFS fitting, and (**d**) oxidation-state analysis [90,91] (reproduced under CC BY 4.0).

5. Advanced Characterization and Theoretical Insights into Reaction Mechanisms

5.1. Ultrafast Spectroscopy for Exciton and Charge Dynamics

The central photophysical question is not whether a COF absorbs light, but what fraction of the initially prepared excited states becomes spatially separated charge that survives long enough to reach a catalytic site. Femtosecond and picosecond transient absorption spectroscopy can resolve ground-state bleaching, stimulated emission, excited-state absorption, charge-transfer-state formation, and long-lived carrier signals across this sequence. In COF-5, ultrafast measurements resolved excimer formation within 4 ± 2 ps, relaxation on a 160 ± 40 ps timescale, and decay beyond 3 ns; fluence-dependent exciton-exciton annihilation yielded a diffusion coefficient of approximately 0.08 $cm^2\ s^{-1}$ and showed that domain size constrains the accessible diffusion distance [6]. In an ordered donor-acceptor COF, electron transfer between segregated columns occurred within approximately 2 ps, demonstrating that periodic heterojunctions can generate long-lived charge-separated states [5]. These foundational observations explain why crystallinity, domain dimensions, layer registry, and donor-acceptor coupling must be considered together rather than inferred from steady-state photoluminescence alone [37].

Temperature-dependent photoluminescence (TDPL) provides a complementary route to estimating E_b, whereas time-resolved photoluminescence reports the decay of emissive states [7,8,27,28]. Neither lifetime extension nor quenching uniquely identifies productive dissociation: a long-lived signal may remain a bound exciton, and quenching may arise from transfer or nonradiative trapping. Mechanistic comparisons should therefore separate three perturbations. Changing imine orientation, dimensionality, stacking, or interlayer coupling tests where the excitation localizes and how it reaches an interface [11–15]; polarizing an Ag-containing site or integrating a metal-framework acceptor tests electron capture after excitation [31,48]; and interlayer Mo coordination, spin coupling, or ionic confinement tests whether the resulting transfer pathway retains usable reducing equivalents [95–97]. Global analysis of transient spectra, fluence dependence, and atmosphere controls should be combined with an independent carrier-extraction measurement before a larger spectroscopic signal is attributed to a larger reactive-carrier population.

Transient surface photovoltage probes directional carrier migration toward an interface, but its amplitude also depends on film thickness, electrode geometry, adsorption, and built-in fields. For Type-II or S-scheme COF heterojunctions, static band-edge estimates should therefore be tested against light-induced potential changes, transfer dynamics, and preservation of the redox potentials required for catalysis [22,29,30,64–67,72,98–103]. Plasmonic Bi- and MXene-containing hybrids require an additional distinction between charge injection, local-field enhancement, and heating [70,71]. Nanoreactors, polarized frameworks, and decorated interfaces address capture and encounter probabilities [50,51,104,105], whereas metal-oxide clusters, porphyrin layers, Resites, and coordinated-metal frameworks change the identity or accessibility of the accepting site [106–110]. These strategies should be compared by the specific step they improve and by product-resolved measurements under matched conditions.

5.2. In Situ/Operando Spectroscopy for Intermediate Monitoring

In situ diffuse reflectance infrared Fourier transform spectroscopy (DRIFTS) is a widely used method for linking COF electronic design to surface chemistry. Under controlled CO_2, water, and illumination, it can follow the adsorption of bicarbonate and carbonate, *COOH or carboxylate-like species, *CO, *OCHO, *CHO, and coupled carbonaceous intermediates. Time-dependent growth and decay are more informative than the presence of a single band because they distinguish a resting adsorbate from a turnover-relevant intermediate. Band assignments should be supported by $^{13}CO_2$-induced frequency shifts, dark-light switching, isotope-sensitive product analysis, and density-functional calculations; overlap among carbonate, solvent, and framework vibrations otherwise creates substantial ambiguity [111,112]. In situ Raman spectroscopy can complement DRIFTS by probing metal-ligand bonding, adsorbate geometry, and framework reconstruction, although fluorescence backgrounds and laser heating require careful control.

Operando X-ray absorption spectroscopy (XAS) adds an atomic-site perspective. X-ray absorption near-edge structure (XANES) can track changes in oxidation state, whereas extended X-ray absorption fine structure (EXAFS) constrains coordination numbers and bond distances. The non-COF examples in Figure 5C, 5E demonstrate why the working site may differ from the as-prepared site [26,90]. For COF photocatalysts, the same question is whether a framework-bound centre persists or becomes a reduced cluster, nanoparticle, or leached species. Comparisons among metal identities, axial ligands, second-sphere polarity, and cooperative sites can connect coordination to *COOH formation or C-C coupling [16,17,20,46,55,56,58–63]. However, calculated adsorption energies and ex situ spectra alone do not prove the proposed light-induced active state. Operando site characterization should therefore be combined with DRIFTS and isotope-validated products, especially for methane and C_{2+} claims [1,41,42,49,52,77,79,80,85].

5.3. DFT Calculations and Microkinetic Modeling

Theory should connect three scales. Periodic electronic-structure calculations describe band dispersion, orbital localization, dielectric response, and interlayer coupling; time-dependent DFT or many-body methods estimate optical excitation and excitonic character; and site-level free-energy calculations evaluate CO_2 adsorption and competing PCET pathways. Difference charge density maps and Bader analysis quantify local electron enrichment. However, the result is model-dependent and must be interpreted using the same coordination, protonation, stacking, and solvent environment as in the experiment. Free-energy diagrams are particularly useful when they compare CO_2 reduction with hydrogen evolution and identify how a structural modification shifts the rate-determining step, rather than merely reporting a favorable isolated adsorption energy [7,16,17,20,46,56,60,62,79]. Figure 5D(c–e) provides a non-COF example: the calculated oxygen-vacancy formation energies in Bi_3TiNbO_9 depend on their orientation relative to ferroelectric polarization (2.955 versus 1.092 eV), and the reported CO_2 adsorption energies are −0.990 and −1.808 eV without and with an oxygen vacancy, respectively [94]. These model energies illustrate defect/adsorption coupling; they cannot be assigned directly to a COF or interpreted as experimental kinetic barriers.

Static diagrams cannot, by themselves, predict selectivity because surface coverage, photon-dependent electron flux, proton activity, product desorption, and competitive site occupation can alter the dominant pathway. Microkinetic modeling can convert elementary barriers into turnover rates and product distributions, reveal transitions between *CO desorption and deeper hydrogenation, and test whether C-C coupling remains feasible at the calculated intermediate coverage. Mechanistic models should therefore be refined iteratively against ultrafast measurements, operando intermediate tracking, and isotope-resolved products. A low calculated barrier with poor activity may reveal insufficient carrier delivery, whereas long-lived carriers with low selectivity may indicate an inappropriate active-site microenvironment.

Table 5 maps each experimental or computational method onto the specific link in the structure–activity chain that it can resolve. Optical and electrical measurements establish energetic feasibility and carrier extraction; ultrafast spectroscopy distinguishes bound excitons, charge-transfer states, and free carriers; operando vibrational and X-ray methods identify intermediates and active-site restructuring; isotope-resolved analytics authenticate the carbon source; and DFT free-energy calculations compare intermediate adsorption and candidate reaction pathways. Kinetic rates and coverages require separate kinetic modelling.

The comparison in Table 5 demonstrates that no single measurement can fully characterize the mechanism. A credible assignment requires temporal evidence that separated charges are formed and survive, spatial or oxidation-state evidence that they reach the proposed active site, operando identification of the relevant adsorbates, and isotope-validated products under matched controls. DFT and microkinetics are more informative when they predict an experimentally observed switch between intermediates or products rather than merely reproducing static band diagrams. Microkinetic modelling remains a prospective approach here. The studies in the DFT free-energy row are not collectively presented as providing rate constants or coverage-dependent models.

Table 5. Methods for mechanistic analysis of COF photocatalysis.

Technique	Detection Target	Key Information Obtained	Typical Limitations	Refs.
Basic band characterization				
UV-vis DRS and Mott-Schottky	Optical gap; band edges	Assesses light harvesting and thermodynamic redox feasibility; supports band-alignment models	Tauc and flat-band assumptions; does not measure productive carriers	[10,13–16,29,31,68,69]
Exciton and charge dynamics characterization				
Steady-state PL/PLQY	Emissive excitons and traps	Relative radiative-loss tendency and environmental quenching	PL quenching is not unique evidence of charge separation	[7,11–14,27,35,56]
TRPL	Excited-state lifetime	Separates fast and slow decay components and compares trapping/recombination	Longer lifetime may represent inactive trapping; model-dependent	[11–16,29,31,68,69]
TDPL	E_b	Arrhenius/thermal activation analysis of bound-exciton dissociation	Requires validated model, spectral assignment, and temperature-independent collection	[12,13,27,35,56]
fs/ps transient absorption	Excitons, CT states, free carriers	Directly resolves exciton formation, dissociation, trapping, transfer, and recombination	Spectral congestion, scattering, fluence dependence, and global-fit ambiguity	[5–7,11–15,35,95]
TPV/TSPV/Kelvin probe	Surface charge separation and migration	Determines charge sign, extraction time, surface potential, and built-in field	Surface-sensitive; contact and atmosphere strongly affect response	[12,15,30,78,86,95]
Photocurrent and EIS	Interfacial carrier collection	Semi-quantitative comparison of transfer resistance and extractable charges	Electrode configuration differs from powder photocatalysis	[10–17,29,31,54,68–71]
EPR/spin trapping	Radicals and unpaired electrons	Identifies photoinduced radicals, spin polarization, and charge accumulation	Spin-trap chemistry may perturb pathways; often qualitative	[11,14,56,70]
In situ/operando intermediate and active-site characterization				

In situ ATR-FTIR/DRIFTS	CO_2 adsorption and surface intermediates	Tracks carbonate species, *COOH, *OCHO, *CO, and *CHO under illumination	Band overlap and adsorption assignments require isotope/DFT support	[15–17,35,54,68,69,109,111]
In situ Raman	Bonding and adsorbate evolution	Monitors framework stability, metal-ligand changes, and selected intermediates	Fluorescence background and laser heating; limited sensitivity	[17,78,111]
XANES/EXAFS	Metal valence and coordination	Reveals dynamic oxidation state, coordination number, and active-site restructuring	Synchrotron access; ensemble averaging; demanding fitting	[16,55,63,86,95,112]
Near-ambient-pressure/operando XPS	Surface chemical states	Tracks surface charge, adsorbates, and oxidation-state changes	Pressure gap, X-ray damage, and shallow probing depth	[78,95,112]
$^{13}CO_2$ labeling+GC-MS/NMR	Carbon origin of products	Authenticates CO, formate, methane, alcohols, and C_2+ products; detects contamination	Requires rigorous gas purification, background subtraction, and isotope-resolved calibration	[15–18,29,54,78,86,110]
		Theoretical calculations		
DFT: band/DOS/charge/Bader	Electronic structure and local electron density	Predicts charge-transfer direction, active-site enrichment, adsorption geometry, and descriptors	Functional/model sensitivity; static structures may not represent operando states	[7,12–17,35,56,68,95,109]
DFT free-energy analysis	Energetic bottlenecks and candidate pathways	Compares intermediate adsorption and reaction free energies; kinetic barriers require separate transition-state calculations	Results depend on functional, solvation, coverage, and proton source; a free-energy diagram alone does not establish kinetic rates or coverages.	[1,15–17,68,78,95,109]

6. Critical Challenges and Future Perspectives

6.1. Degradation Mechanisms: Photochemical and Chemical Stability

Stability must be separated into chemical and photochemical components. Chemical degradation is dominated by linkage hydrolysis, nucleophile or acid/base attack, metal decoordination, and swelling-induced loss of order. Photochemical degradation can proceed through oxidation of imine or enamine motifs by holes or reactive oxygen species, reduction of linkages by accumulated electrons, chromophore bleaching, and irreversible radical chemistry. Imine-linked COFs often provide crystallinity but limited hydrolytic robustness. In contrast, β-ketoenamine, vinylene, sp^2-carbon, amide, and post-converted linkages generally improve resistance at the cost of different synthetic or electronic tradeoffs [19,21,113,114]. Functionalization, Doebner conversion, ether incorporation, cluster crosslinking, and donor-π-acceptor linkages demonstrate that stability and charge transport should be co-optimized rather than treated independently [10,35,36,43,47,87].

A stable powder pattern after cycling is insufficient evidence. Post-reaction powder X-ray diffraction (PXRD) and spectroscopy should be combined with porosity, microscopy, elemental analysis, metal-leaching measurements, solution-phase organic analysis, and carbon balance. Heterojunctions require additional checks for interface delamination, cocatalyst sintering, and phase transformation. For organic photocatalysts, isotope tracing must also verify that carbon products do not arise from framework decomposition. Long-duration, intermittent-light, and start-stop tests are more informative than a few short recycling runs because they expose slow hydrolysis, the accumulation of strongly bound intermediates, and limitations in regeneration.

6.2. Standardized Testing Protocols and Data Reliability

Reliable comparison requires a minimum reporting set: catalyst mass and illuminated area; reactor volume and phase configuration; CO_2 purity and flow or pressure; water and sacrificial-donor composition; cocatalyst and photosensitizer loading; lamp spectrum and calibrated irradiance; temperature; mixing; sampling schedule; analytical calibration; replicate number; and uncertainty. Rates should be reported both per catalyst mass and as absolute formation amounts, together with selectivity definitions and electron balance. AQY must use monochromatic incident photon flux and the stoichiometric electron number of every product; it must not be presented as solar-to-fuel efficiency.

The carbon source requires $^{13}CO_2$ tracing with chromatographic separation capable of distinguishing isotopologues, matched $^{12}CO_2$ experiments, and no-light, no-catalyst, and no-CO_2 or inert-gas controls. Isotope purity, residual air, carrier gases, tubing contamination, solvents, sacrificial agents, and catalyst pretreatment can all compromise interpretation. Rigorous protocols have shown that isotope tracing is not automatically conclusive when products and reactants are not adequately separated or when unlabeled carbon reservoirs are ignored [18]. Raw chromatograms, mass spectra, calibration curves, and blank signals should therefore be deposited as supporting data.

6.3. Scalability and Device Application Barriers

Practical deployment is constrained by more than photocatalytic rate. COF synthesis must be reproducible at larger batch sizes with controlled crystallinity, linkage conversion, defect density, and metal-site loading; the catalyst must then be recoverable without pore collapse, delamination, or metal leaching. At high CO_2 loading, photon penetration through concentrated suspensions or thick films, gas–liquid mass transfer, and local depletion of CO_2 can become rate-limiting. Reactor scale-up should therefore report optical

path length, illuminated volume, photon flux, gas residence time, mixing, and continuous product removal, rather than extrapolating a batch rate directly to device productivity.

Scale-up introduces constraints that are largely absent from milligram batch tests. Multistep monomer synthesis, dilute solvothermal conditions, toxic solvents, long crystallization times, and batch-dependent defect densities increase cost and variability. At reactor scale, powder scattering and self-shading limit photon penetration, while CO_2 solubility, water management, product removal, and gas–liquid mass transfer can dominate the apparent kinetics. Immobilized films, membranes, monoliths, and three-dimensional or Q1D frameworks may shorten transport distances and simplify catalyst recovery, but often sacrifice accessible surface area or introduce contact resistance [15,32,55,63,98].

Device-oriented development should therefore integrate synthesis and reactor design. Continuous-flow gas-diffusion photoreactors can decouple CO_2 delivery from bulk solubility; thin COF coatings can reduce optical thickness; conductive supports can provide directional extraction; and membrane architectures can combine capture, enrichment, and reaction. Performance must be evaluated under concentrated or dilute CO_2, humid feeds, oxygen impurities, extended illumination, and realistic photon flux. Volumetric productivity, area-normalized solar conversion, pressure drop, catalyst lifetime, and separation energy will ultimately be more relevant than a short-term mass-normalized rate.

6.4. Promising Research Directions

Future progress requires descriptor-driven co-design across the complete reaction chain. E_b should be measured together with exciton diffusion length, free-carrier yield, and interfacial transfer rate; active sites should be screened by local charge, adsorption-energy windows, and proton-delivery geometry; and pore environments should be designed for the targeted product rather than maximum CO_2 uptake alone. High-throughput computation and automated synthesis can identify Pareto-optimal frameworks that balance dissociation, redox driving force, stability, and selectivity. Multimodal operando cells that combine transient optical spectroscopy, vibrational probes, XAS, and online isotope-resolved analytics are needed to observe structural and chemical dynamics under the same conditions.

Recent studies illustrate several complementary directions. Atomic Mo–N4 interlayer bridges were used to accelerate vertical electron transfer while activating CO_2 [95]; continuous high-spin orbital coupling connected a COF excited state to a Ni catalytic center and lowered a reported rate-determining barrier [96]; electrostatic confinement in an ionic COF promoted forward transfer to a cationic Co complex [97]. Other studies pursued confined C_{60} nanoreactors [104], metal–COF oxide clusters [106], decorated COFs with stronger CO_2 interaction [105], noble-metal-free porphyrin COF layers [107], and triazine–benzene linkage engineering that couples charge separation with *COOH stabilization [109]. These examples support a common design principle: exciton and interface engineering should be evaluated together with active-site identity and intermediate energetics.

For deep C_1 and C_{2+} products, asymmetric neighboring sites, controlled intermediate confinement, and sustained electron flux should be developed simultaneously [50,80,84,104]. Tandem COF architectures may separate light absorption, oxidation, CO generation, coupling, and hydrogenation into spatially organized modules, while photothermal and photoelectrochemical assistance can relieve individual kinetic bottlenecks. The field should nevertheless resist complexity without mechanistic gain: every added junction, cluster, or field must be justified by a quantitative improvement in a defined step. Shared data standards and reference materials will be essential for converting increasingly sophisticated molecular design into reproducible solar-fuel devices.

Machine learning can become useful for COF photocatalysis only after the experimental record is standardized. Models can combine framework descriptors, E_b or charge-transfer observables, pore and active-site features, light input, reactor variables, and product-analysis metadata to identify transferable structure–condition descriptors. Recent hybrid experimental/ML work used catalyst characteristics and operational parameters to predict CO_2 photoreduction performance and used Shapley additive explanations (SHAP) analysis to identify dominant variables, while a COF study showed that data augmentation, ensemble modelling, and mechanism-informed descriptors can address sparse datasets. The key limitations remain dataset heterogeneity, domain shift between reactor platforms, descriptor leakage, and weak causal interpretability. Active learning linked to operando spectroscopy and isotope-validated experiments is therefore more credible than a rate-only black-box ranking.

7. Conclusions

COFs provide a structurally programmable platform for photocatalytic CO_2 reduction because their chromophores, linkages, stacking modes, pores, interfaces, and catalytic sites can be controlled within one periodic architecture. The evidence reviewed here indicates that the primary physical bottleneck is not light absorption alone, but rather the coupled generation and use of free carriers. Quantitative regulation of E_b, diffusion, dissociation, and interfacial transfer is therefore the foundation for improving catalytic efficiency. Conjugation, donor-acceptor polarization, layer geometry, dimensionality, and heterojunctions are valuable only when they increase the electron population delivered to a chemically competent site before recombination.

Product selectivity is governed at the next level by local electron density, proton supply, pore confinement, and intermediate adsorption. CO formation requires efficient *COOH generation and controlled *CO release; formate requires stabilization of *OCHO; methane requires sustained multielectron PCET; and C_{2+} synthesis requires adjacent, electronically asymmetric sites that maintain coupling-competent intermediate coverage. These chemical requirements explain why improved charge separation does not automatically yield the desired product. Predictive design must connect photophysical descriptors to adsorption energies, rate-determining states, and microkinetic product distributions.

The field now needs fewer isolated performance claims and more convergent evidence. Ultrafast spectroscopy, operando DRIFTS and XAS, isotope-resolved product analysis, DFT, and microkinetic modeling should be applied under comparable conditions. Rigorous $^{13}CO_2$ tracing, calibrated photon input, complete blank controls, transparent normalization, and long-term degradation analysis are indispensable. With these standards, the central structure-activity chain consisting of framework engineering, exciton dissociation, carrier transfer, active-site electron density, intermediate energetics, and selectivity can become a predictive basis for scalable COF photocatalysts rather than a retrospective explanation of individual materials.

Author Contributions: Conceptualization, D.X., N.S. and H.Z.; Software, D.X., B.M., X.F., L.J., X.L. and C.Y.; Validation, X.F., N.S., X.L. and C.Y.; Data Curation, D.X., B.M., X.F., L.J. and X.L.; Writing—Original Draft Preparation, D.X., B.M., X.F. and C.Y.; Writing—Review and Editing, D.X., N.S., X.L. and H.Z.; Visualization, L.J., N.S. and X.L.; Resources, N.S., H.Z.; Funding Acquisition, D.X., C.Y. and H.Z. All authors have read and agreed to the published version of the manuscript.

Funding: We acknowledge the Central Public-interest Scientific Institution Basal Research Fund (NO. GYZX20260204, GYZX20260312) , the Financial Budget Project of the Ministry of Ecology and Environment, and the Special Fund of the Carbon Peak and Carbon Neutrality Research Institute that is supported by the Nanjing Institute of Environmental Sciences, Ministry of Ecology and Environment (ZX2023SZY060).

Data Availability Statement: No new data were created or analyzed in this review. Data sharing does not apply to this article.

Conflicts of Interest: Author Xiuzhen Fan was employed by the company Shandong Haipuou Environmental Protection Equipment Technology Co., Ltd. The remaining authors declare that the research was conducted in the absence of any commercial or financial relationships that could be construed as a potential conflict of interest.

Abbreviations

The following abbreviations are used in this manuscript:

Abbreviation	Definition
1D	one-dimensional
2D	two-dimensional
3D	three-dimensional
AQY	apparent quantum yield
ATR-FTIR	attenuated total reflectance Fourier-transform infrared spectroscopy
BET	Brunauer–Emmett–Teller
C_1	one-carbon product class
C_{2+}	products containing two or more carbon atoms
COFs	covalent organic frameworks
D–A	donor–acceptor
D–A–C	donor–acceptor–catalytic site
DFT	density functional theory
DOS	density of states
DRIFTS	diffuse reflectance infrared Fourier-transform spectroscopy
E_b	exciton binding energy
EIS	electrochemical impedance spectroscopy
EPR	electron paramagnetic resonance
EXAFS	extended X-ray absorption fine structure
fs	femtosecond
GC-MS	gas chromatography–mass spectrometry
GW–BSE	GW approximation–Bethe–Salpeter equation
HER	hydrogen evolution reaction
HOMO	highest occupied molecular orbital
ICT	intramolecular charge transfer
LDH	layered double hydroxide
LSPR	localized surface plasmon resonance
LUMO	lowest unoccupied molecular orbital
MOFs	metal–organic frameworks
MS	mass spectrometry
NMR	nuclear magnetic resonance
NR	not reported
PCET	proton-coupled electron transfer
PL	photoluminescence
PLQY	photoluminescence quantum yield
PS	photosensitizer
ps	picosecond
PXRD	powder X-ray diffraction
Q1D	quasi-one-dimensional
RDS	rate-determining step

TDPL	temperature-dependent photoluminescence
TRPL	time-resolved photoluminescence
TPV	transient photovoltage
TSPV	transient surface photovoltage
UV–vis DRS	ultraviolet–visible diffuse reflectance spectroscopy
XANES	X-ray absorption near-edge structure
XAS	X-ray absorption spectroscopy
XPS	X-ray photoelectron spectroscopy

References

1. Li, Z.; Yang, X.; Zhang, Z.; Xiong, Y.; Zou, Z.; Zhou, Y. Engineering product selectivity in photocatalytic CO_2 reduction: Fundamentals, mechanisms, and catalyst design. *Chem. Commun.* **2026**, *62*, 7490–7504. https://doi.org/10.1039/D6CC00798H.
2. Essalhi, M.; Mahmoud, E.-H.; Tayeb, A.; Al-Qahtani, R.A.; Farooqi, A.S.; Abdelnaby, M. Structural design of covalent organic frameworks and their recent advancements in carbon capture applications: A review. *Carbon Capture Sci. Technol.* **2025**, *14*, 100370. https://doi.org/10.1016/j.ccst.2025.100370.
3. Zhao, K.; Quan, X. Carbon-Based Materials for Electrochemical Reduction of CO_2 to C_{2+} Oxygenates: Recent Progress and Remaining Challenges. *ACS Catal.* **2021**, *11*, 2076–2097. https://doi.org/10.1021/acscatal.0c04714.
4. Ahmed, S.; Khan, M.K.; Kim, J. Revolutionary advancements in carbon dioxide valorization via metal-organic framework-based strategies. *Carbon Capture Sci. Technol.* **2025**, *15*, 100405. https://doi.org/10.1016/j.ccst.2025.100405.
5. Jin, S.; Ding, X.; Feng, X.; Supur, M.; Furukawa, K.; Takahashi, S.; Addicoat, M.; El-Khouly, M.E.; Nakamura, T.; Irle, S.; et al. Charge Dynamics in A Donor–Acceptor Covalent Organic Framework with Periodically Ordered Bicontinuous Heterojunctions. *Angew. Chem. Int. Ed.* **2013**, *52*, 2017–2021. https://doi.org/10.1002/anie.201209513.
6. Flanders, N.C.; Kirschner, M.S.; Kim, P.; Fauvell, T.J.; Evans, A.M.; Helweh, W.; Spencer, A.P.; Schaller, R.D.; Dichtel, W.R.; Chen, L.X. Large Exciton Diffusion Coefficients in Two-Dimensional Covalent Organic Frameworks with Different Domain Sizes Revealed by Ultrafast Exciton Dynamics. *J. Am. Chem. Soc.* **2020**, *142*, 14957–14965. https://doi.org/10.1021/jacs.0c05404.
7. Qian, Y.; Han, Y.; Zhang, X.; Yang, G.; Zhang, G.; Jiang, H.-L. Computation-based regulation of excitonic effects in donor-acceptor covalent organic frameworks for enhanced photocatalysis. *Nat. Commun.* **2023**, *14*, 3083. https://doi.org/10.1038/s41467-023-38884-w.
8. Qian, Y.; Li, D.; Han, Y.; Jiang, H.-L. Photocatalytic Molecular Oxygen Activation by Regulating Excitonic Effects in Covalent Organic Frameworks. *J. Am. Chem. Soc.* **2020**, *142*, 20763–20771. https://doi.org/10.1021/jacs.0c09727.
9. Côté, A.P.; Benin, A.I.; Ockwig, N.W.; O'Keeffe, M.; Matzger, A.J.; Yaghi, O.M. Porous, Crystalline, Covalent Organic Frameworks. *Science* **2005**, *310*, 1166–1170. https://doi.org/10.1126/science.1120411.
10. Yang, L.; Yan, W.; Yang, N.; Wang, G.; Bi, Y.; Tian, C.; Liu, H.; Zhu, X. Regulating π-Conjugation in sp^2-Carbon-Linked Covalent Organic Frameworks for Efficient Metal-Free CO_2 Photoreduction with H_2O. *Small* **2023**, *19*, 2208118. https://doi.org/10.1002/smll.202208118.
11. Streater, D.H.; Kennehan, E.R.; Wang, D.; Fiankor, C.; Chen, L.; Yang, C.; Li, B.; Liu, D.; Ibrahim, F.; Hermans, I.; et al. Control over Charge Separation by Imine Structural Isomerization in Covalent Organic Frameworks with Implications on CO_2 Photoreduction. *J. Am. Chem. Soc.* **2024**, *146*, 4489–4499. https://doi.org/10.1021/jacs.3c10627.
12. Qin, L.; Sun, D.; Ma, D.; Wang, Z.; Liu, Y.; Li, Q.; Song, F.; Wu, K.; Gan, L.; Zhou, T.; et al. Decoupling Interlayer Interactions Boosts Charge Separation in Covalent Organic Frameworks for High-Efficiency Photocatalytic CO_2 Reduction. *Adv. Mater.* **2025**, *37*, 2504205. https://doi.org/10.1002/adma.202504205.
13. Liu, Y.; Chi, W.; He, Y.-O.; Zhu, R.-M.; Feng, J.-D.; Zhu, K.; Zhang, J.; Pang, H.; Han, Y.; Han, W.-K.; et al. Twisted Stacking 2D Covalent Organic Frameworks with Directional Electron Transport for Boosting CO_2 Photoreduction. *ACS Nano* **2026**, *20*, 17721–17734. https://doi.org/10.1021/acsnano.6c05729.
14. Wang, X.; Zhang, H.; Zheng, X.; Cui, J.; Yu, M.; Liu, H.; Zhao, Y. Dimensional Isomerism in COFs Enabled by Spirobifluorene Substitution for Enhanced Photocatalytic CO_2 Reduction. *Angew. Chem. Int. Ed.* **2026**, *65*, e1182476. https://doi.org/10.1002/anie.1182476.
15. Bai, J.; Hu, Y.; Si, F.; Li, Y.; Liang, G.; Hou, T.; Li, Y. Quasi-one-dimensional enaminone-linked covalent organic frameworks for efficient CO_2 photoreduction. *Nat. Commun.* **2026**, *17*, 2158. https://doi.org/10.1038/s41467-026-69361-9.
16. Zhou, M.; Wang, Z.; Mei, A.; Yang, Z.; Chen, W.; Ou, S.; Wang, S.; Chen, K.; Reiss, P.; Qi, K.; et al. Photocatalytic CO_2 reduction using La-Ni bimetallic sites within a covalent organic framework. *Nat. Commun.* **2023**, *14*, 2473. https://doi.org/10.1038/s41467-023-37545-2.

17. Chen, X.; Xie, W.; Yang, L.; Cheng, Y.; Zhang, R.; Zhang, Q.; Deng, W.-Q.; Liu, C. A High-Performance Rh-TMP-COF Photocatalyst for CO_2-to-CO Conversion with H_2O Vapor: From Descriptor Prediction to Experimental Validation. *J. Am. Chem. Soc.* **2026**, *148*, 19835–19844. https://doi.org/10.1021/jacs.6c02264.
18. Wang, S.; Jiang, B.; Henzie, J.; Xu, F.; Liu, C.; Meng, X.; Zou, S.; Song, H.; Pan, Y.; Li, H.; et al. Designing reliable and accurate isotope-tracer experiments for CO_2 photoreduction. *Nat. Commun.* **2023**, *14*, 2534. https://doi.org/10.1038/s41467-023-38052-0.
19. Nguyen, H.L.; Alzamly, A. Covalent Organic Frameworks as Emerging Platforms for CO_2 Photoreduction. *ACS Catal.* **2021**, *11*, 9809–9824. https://doi.org/10.1021/acscatal.1c02459.
20. Rath, B.B.; Krause, S.; Lotsch, B.V. Active Site Engineering in Reticular Covalent Organic Frameworks for Photocatalytic CO_2 Reduction. *Adv. Funct. Mater.* **2024**, *34*, 2309060. https://doi.org/10.1002/adfm.202309060.
21. Yang, X.; Xu, Q.; Wei, W.; Zeng, G. Linkages Chemistry of Covalent Organic Frameworks in Photocatalysis and Electrocatalysis. *Angew. Chem. Int. Ed.* **2025**, *64*, e202504355. https://doi.org/10.1002/anie.202504355.
22. Li, Q.; Li, X.; Zhang, B.; Jiang, B. Recent Advancements in COFs-Based Heterostructures for CO_2 Photoreduction. *Adv. Funct. Mater.* **2025**, *35*, 2506421. https://doi.org/10.1002/adfm.202506421.
23. Che, W.; Zhao, S.; Byun, W.J.; Tao, T.; Jeon, J.P.; Zhao, Q.; Shao, Y.; Li, J.; Kim, J.; Lee, J.S.; et al. From Carbon Nitrides to COFs: Opportunities and Prospects in Photocatalytic CO_2 Reduction. *Adv. Mater.* **2025**, *37*, e06961. https://doi.org/10.1002/adma.202506961.
24. Cheng, K.; Kong, S.; Wang, J.; Wang, Q.; Yuan, S.; Li, P.Z.; Zhao, Y. Integrating Multifunctionalities into a 3D Covalent Organic Framework for Efficient CO_2 Photoreduction. *Angew. Chem. Int. Ed.* **2025**, *64*, e202504772. https://doi.org/10.1002/anie.202504772.
25. Ding, L.; Harikrishnan, L.; Liu, S.; Pitcheri, R.; Qi, K. Covalent organic framework-based S-scheme photocatalysts: Mechanistic insights and emerging applications in energy and environment. *Nano Mater. Sci.* **2026**. https://doi.org/10.1016/j.nanoms.2026.01.004.
26. Lin, S.-C.; Chang, C.-C.; Chiu, S.-Y.; Pai, H.-T.; Liao, T.-Y.; Hsu, C.-S.; Chiang, W.-H.; Tsai, M.-K.; Chen, H.M. Operando time-resolved X-ray absorption spectroscopy reveals the chemical nature enabling highly selective CO_2 reduction. *Nat. Commun.* **2020**, *11*, 3525. https://doi.org/10.1038/s41467-020-17231-3.
27. Wang, X.X.; Zhang, C.R.; Bi, R.X.; Peng, Z.H.; Song, A.M.; Zhang, R.; He, H.X.; Qi, J.X.; Gong, J.W.; Niu, C.P.; et al. Reducing the Exciton Binding Energy of Covalent Organic Framework Through π-Bridges to Enhance Photocatalysis. *Adv. Funct. Mater.* **2025**, *35*, 2421623. https://doi.org/10.1002/adfm.202421623.
28. Xu, Q.; Li, Y.; Jin, Z.; Yu, X.; Cao, F.; Xue, S.; Liu, H.; Wagner, M.; Müllen, K.; Zhi, L. Reducing Exciton Binding Energy in 2D Covalent Organic Frameworks by Decreasing Layer Planarity. *Adv. Funct. Mater.* **2026**, *36*, e16937. https://doi.org/10.1002/adfm.202516937.
29. Ou, S.; Zhou, M.; Chen, W.; Zhang, Y.; Liu, Y. COF-5/CoAl-LDH Nanocomposite Heterojunction for Enhanced Visible-Light-Driven CO_2 Reduction. *ChemSusChem* **2022**, *15*, e202200184. https://doi.org/10.1002/cssc.202200184.
30. Niu, Q.; Dong, S.; Tian, J.; Huang, G.; Bi, J.; Wu, L. Rational Design of Novel COF/MOF S-Scheme Heterojunction Photocatalyst for Boosting CO_2 Reduction at Gas–Solid Interface. *ACS Appl. Mater. Interfaces* **2022**, *14*, 24299–24308. https://doi.org/10.1021/acsami.2c02439.
31. Chen, Y.; Zheng, S.; Huang, X.; Zhang, Z.; Huang, G.; Chen, Q.; Wu, L.; Bi, J. Interlayer polarization induced by Ag–N2 motifs in spherical covalent organic framework driving efficient CO_2 photoreduction. *J. Mater. Chem. A* **2026**, *14*, 16571–16580. https://doi.org/10.1039/D5TA10283A.
32. Mohata, S.; Majumder, P.; Banerjee, R. Design and structure–function interplay in covalent organic frameworks for photocatalytic CO_2 reduction. *Chem. Soc. Rev.* **2025**, *54*, 6062–6087. https://doi.org/10.1039/D5CS00106D.
33. Xue, D.; Yan, X.; Liu, F.; Liu, M.; Zhang, H. Anthrathiophene-Based Covalent Organic Frameworks with Powerful π-Conjugation toward High-Efficiency CO_2 Photoconversion. *ACS Appl. Mater. Interfaces* **2025**, *17*, 63467–63477. https://doi.org/10.1021/acsami.5c17594.
34. Lei, T.; Mi, Y.; Wei, Z.; Li, S.; Pang, S. Application of fully conjugated covalent organic frameworks in photocatalytic carbon dioxide reduction performance. *Dalton Trans.* **2023**, *52*, 1761–1767. https://doi.org/10.1039/D2DT03743B.
35. Wang, Z.; Wang, X.F.; Hu, T.L.; Zhang, Y.H. Synergistic Modulation of Photoexcitation Dynamics and Catalytic Site Activation in Covalent Organic Frameworks through Doebner Nonconjugated Modification for Boosting Photocatalytic CO_2 Reduction. *Small* **2026**, *22*, e14818. https://doi.org/10.1002/smll.202514818.
36. Li, X.; Jiang, K.; Li, M.; Meng, F.; Li, J.; Yang, K.; Xue, B.; Zhuang, X.; Wu, D.; Zhang, F. Bipyrimidine-Boosted Preparation and Post-Functionalization of Vinylene-Linked Covalent Organic Frameworks for Sacrificial-Agent-Free Photocatalysis of CO_2 Reduction. *Small* **2026**, *22*, e73308. https://doi.org/10.1002/smll.73308.

37. Streater, D.; Hu, W.; Kelley, M.S.; Yang, S.; Kohlstedt, K.L.; Huang, J. Wavelength-Dependent Excitonic Properties of Covalent Organic Frameworks Explored by Theory and Experiments. *J. Phys. Chem. C* **2023**, *127*, 12321–12332. https://doi.org/10.1021/acs.jpcc.3c02296.
38. Elgharpawy, A.; Alzard, M.H.; Alzard, R.H.; Morsi, R.; Chen, D.; Niu, F.; Al Neyadi, S.; Abdellah, M. COF-based photocatalysis: Global research dynamics, synthetic approaches, and future directions revealed through a scientometric analysis from 2015 to 2025. *Mater. Today Sustain.* **2026**, *35*, 101388. https://doi.org/10.1016/j.mtsust.2026.101388.
39. Ma, Y.; Zhang, Q.; Chen, H.; Wang, H.; Deng, Y.; Guo, Y.; Gao, S.; Wang, J. Rational regulation of the torsion angle of covalent organic frameworks for enhanced CO_2 photoreduction to ethane. *Chem. Sci.* **2026**, *17*, 11627–11636. https://doi.org/10.1039/D5SC09241H.
40. Li, C.; Liu, J.; Li, H.; Wu, K.; Wang, J.; Yang, Q. Covalent organic frameworks with high quantum efficiency in sacrificial photocatalytic hydrogen evolution. *Nat. Commun.* **2022**, *13*, 2357. https://doi.org/10.1038/s41467-022-30035-x.
41. He, J.; Wang, Z.; Xue, J.; Huang, B.; Yang, L.; Luo, C.; Cui, X.; Ji, Z.; Sheng, D.; Chen, T.; et al. Engineering the Electronic Microenvironment with Bromine Functionalization for High-Selectivity Photocatalytic CO_2 Reduction. *Small* **2026**, *22*, e13767. https://doi.org/10.1002/smll.202513767.
42. Zhang, Y.; Zang, L.; Zhao, S.; Cheng, W.; Zhang, L.; Sun, L. Brominated metal phthalocyanine-based covalent organic framework for enhanced selective photocatalytic reduction of CO_2. *J. Colloid. Interface Sci.* **2024**, *655*, 1–11. https://doi.org/10.1016/j.jcis.2023.10.111.
43. Zhou, D.; Chen, Q.; Zhang, J.; Wang, T.; Liu, Z.Q. Ether-Embedded Covalent Organic Frameworks Enable Efficient Photocatalytic CO_2 Reduction. *Angew. Chem. Int. Ed.* **2025**, *64*, e202500329. https://doi.org/10.1002/anie.202500329.
44. Que, Y.T.; Zhu, R.M.; Liu, Y.; He, Y.O.; Han, W.K.; Pang, H.; Zhang, J.; Gu, Z.G. Engineering Proton Clamp Traps in Covalent Organic Frameworks for Boosting CO_2 Capture and Photoreduction. *Angew. Chem. Int. Ed.* **2025**, *64*, e15511. https://doi.org/10.1002/anie.202515511.
45. He, Y.; Zhao, Y.; Wang, X.; Liu, Z.; Yu, Y.; Li, L. Multiple Heteroatom-Hydrogen Bonds Bridging Electron Transport in Covalent Organic Framework-Based Supramolecular System for Photoreduction of CO_2. *Angew. Chem.* **2023**, *135*, e202307160. https://doi.org/10.1002/ange.202307160.
46. Zhang, S.-W.; Zheng, W.-Y.; Hu, S.-Z.; Mao, Q.-R.; Tian, M.; Han, W.-K.; Gu, Z.-G. Metal covalent organic frameworks with donor-acceptor-catalytic site (D-A-C) for boosting CO_2 photoreduction. *Chem. Eng. J.* **2026**, *544*, 179045. https://doi.org/10.1016/j.cej.2026.179045.
47. Li, S.; Gao, C.; Yu, H.; Wang, Y.; Wang, S.; Ding, W.; Zhang, L.; Yu, J. Vinylene-Linked Donor-π-Acceptor Metal-Covalent Organic Framework for Enhanced Photocatalytic CO_2 Reduction. *Angew. Chem. Int. Ed.* **2024**, *63*, e202409925. https://doi.org/10.1002/anie.202409925.
48. Han, W.-K.; Li, J.; Zhu, R.-M.; Wei, M.; Xia, S.-K.; Fu, J.-X.; Zhang, J.; Pang, H.; Li, M.-D.; Gu, Z.-G. Photosensitizing metal covalent organic framework with fast charge transfer dynamics for efficient CO_2 photoreduction. *Chem. Sci.* **2024**, *15*, 8422–8429. https://doi.org/10.1039/D4SC01896F.
49. Wang, Y.; Yang, F.; Liu, S.; Chen, J.; Cai, Y.; Zhang, G.; Yang, X.; Qu, J.; Hu, J. Acceptor-tailored olefin-linked covalent organic frameworks for highly selective CO_2 photoreduction to methane. *Chem. Eng. J.* **2026**, *537*, 172259. https://doi.org/10.1016/j.cej.2025.172259.
50. Wang, X.; Li, X.; Li, M.; Li, Z.; Lei, Z.; Huang, S.; Yi, J.; Yuan, Z.-Y.; Ye, L.; Cui, W.-G.; et al. Polarisation Engineering in Covalent Organic Frameworks for Catalysis. *Nano-Micro Lett.* **2026**, *18*, 347. https://doi.org/10.1007/s40820-026-02183-y.
51. Li, Y.; Wang, L.; Fan, D.; Li, Z.; Zhao, C.; Yang, X. Enhanced Photocatalytic Reduction of CO_2 to Complete CO Mediated by Donor–Acceptor Covalent Organic Frameworks. *Energy Environ. Mater.* **2026**, *9*, e70150. https://doi.org/10.1002/eem2.70150.
52. Wang, J.; Han, C.; Ye, L. Position-dependent carboxyl functionalization in covalent organic frameworks for selective photocatalytic CO_2 reduction. *Front. Chem.* **2026**, *14*, 1892359. https://doi.org/10.3389/fchem.2026.1892359.
53. Lu, C.J.; Zhang, J.H.; Mei, J.H.; Gong, Y.N.; Lu, T.B.; Zhong, D.C. Modulating the Chromophores of Metal-Covalent Organic Frameworks for Boosting Low-Concentration CO_2 Photoreduction. *Angew. Chem. Int. Ed.* **2025**, *64*, e202505292. https://doi.org/10.1002/anie.202505292.
54. Yang, Y.; Zhang, H.Y.; Wang, Y.; Shao, L.H.; Fang, L.; Dong, H.; Lu, M.; Dong, L.Z.; Lan, Y.Q.; Zhang, F.M. Integrating Enrichment, Reduction, and Oxidation Sites in One System for Artificial Photosynthetic Diluted CO_2 Reduction. *Adv. Mater.* **2023**, *35*, 2304170. https://doi.org/10.1002/adma.202304170.

55. Gao, S.; Zhao, X.; Zhang, Q.; Guo, L.; Li, Z.; Wang, H.; Zhang, S.; Wang, J. Mimic metalloenzymes with atomically dispersed Fe sites in covalent organic framework membranes for enhanced CO_2 photoreduction. *Chem. Sci.* **2025**, *16*, 1222–1232. https://doi.org/10.1039/D4SC05999A.
56. Chen, Y.; Chen, S.; Yu, M.; Huang, G.; Chen, Q.; Wu, L.; Li, L.; Bi, J. Regulating Electronic Structure of Transition Metal Single-Atoms in COFs for Enhanced Photocatalytic CO_2 Reduction. *Adv. Mater.* **2026**, *38*, e73738. https://doi.org/10.1002/adma.73738.
57. Zhang, Q.; Chen, M.; Zhang, Y.; Ye, Y.; Liu, D.; Xu, C.; Ma, Z.; Lou, B.; Yuan, R.; Sa, R. Iron/cobalt/nickel regulation for efficient photocatalytic carbon dioxide reduction over phthalocyanine covalent organic frameworks. *Nanoscale* **2023**, *15*, 16030–16038. https://doi.org/10.1039/D3NR04387H.
58. Dai, N.; Qian, Y.; Wang, D.; Huang, J.; Guan, X.; Lin, Z.; Yang, W.; Wang, R.; Huang, J.; Zang, S.-Q.; et al. Regulation of Coordinating Anions around Single Co(II) Sites in a Covalent Organic Framework for Boosting CO_2 Photoreduction. *Precis. Chem.* **2024**, *2*, 600–609. https://doi.org/10.1021/prechem.4c00058.
59. Zhang, Y.; Cao, L.; Bai, G.; Lan, X. Engineering Single Cu Sites into Covalent Organic Framework for Selective Photocatalytic CO_2 Reduction. *Small* **2023**, *19*, 2300035. https://doi.org/10.1002/smll.202300035.
60. Wang, P.; Dai, Y.; Song, Z.; Wang, Y.; Wei, J.; Liu, Z.; Ma, Y.; Yang, F.; Qu, J.; Liu, S.; et al. Polarized microenvironment-modulated covalent organic frameworks with nickel single atoms for enhanced CO_2 photoreduction. *Chem. Eng. J.* **2025**, *511*, 162084. https://doi.org/10.1016/j.cej.2025.162084.
61. Xia, S.K.; Liu, Y.; Zhu, R.M.; Feng, J.D.; Han, W.K.; Gu, Z.G. 1D Covalent Organic Frameworks with Tunable Dual-Cobalt Synergistic Sites for Efficient CO_2 Photoreduction. *Macromol. Rapid Commun.* **2025**, *46*, 2400780. https://doi.org/10.1002/marc.202400780.
62. Hu, Y.; Zhang, H.; Xie, X.; Li, Y.; Song, T.; Hu, X.; Long, B.; Deng, G.-J. Dual modulation of metal center and pore topology in covalent organic frameworks for photoreduction of carbon dioxide to multi-carbon fuels. *J. Colloid. Interface Sci.* **2025**, *700*, 138510. https://doi.org/10.1016/j.jcis.2025.138510.
63. Ai, L.Y.; Wang, Q.; Chen, X.W.; Jiang, G.F. One-dimensional phenanthroline-based covalent organic framework bearing single cobalt atoms for efficient photocatalytic CO_2 reduction. *Aggregate* **2024**, *5*, e582. https://doi.org/10.1002/agt2.582.
64. Niu, Q.; Chen, Q.; Huang, G.; Li, L.; He, Y.; Bi, J. Build-in electric field in CuWO4/covalent organic frameworks S-scheme photocatalysts steer boosting charge transfer for photocatalytic CO_2 reduction. *J. Colloid. Interface Sci.* **2023**, *643*, 102–114. https://doi.org/10.1016/j.jcis.2023.04.013.
65. Mu, M.; Meng, L.; Ma, S.; Chen, W.; Yin, X.; Bai, G. Interfacial imine-bridging and charge directional migration dual regulation of ZnO/covalent organic frameworks S-scheme heterostructure for boosting photocatalytic CO_2 reduction. *J. Colloid. Interface Sci.* **2025**, *686*, 63–74. https://doi.org/10.1016/j.jcis.2025.01.232.
66. Liu, C.; Gao, T.; Wang, G.; Cheng, Q.; Wang, K. Efficient CO_2 Photoreduction into Solar Fuels over MoO3−x/COF S-Scheme Photocatalyst. *Chem. Res. Chin. Univ.* **2025**, *41*, 726–733. https://doi.org/10.1007/s40242-025-5033-9.
67. Wang, X.; Wang, Z.; Liu, Y.; Peng, W.; Fu, X.; Zhou, J.; Han, L.; Hua, Y.; Zhou, Z.-Y. A multi-centre metal-free COF@g-C3N4 catalyst assembled with covalent bonds for photocatalytic CO_2 reduction. *Dalton Trans.* **2025**, *54*, 1625–1632. https://doi.org/10.1039/D4DT02996H.
68. Sun, B.; Zhao, X.; Meng, Z.; Wang, D.; Bu, X.-H. L-cysteine-bridged $Bi_3TiNbO_{8.5}F$@COF-2CN heterojunction for selective photocatalytic CO_2-to-HCOOH conversion. *J. Colloid. Interface Sci.* **2026**, *724*, 141102. https://doi.org/10.1016/j.jcis.2026.141102.
69. Chen, Y.; Liang, T.; Lin, Y.; Peng, W.; Chen, Z.; Lin, W.; Sham, Y.-T.; Pan, M.; Chen, Q.; Huang, G.; et al. Enhanced photocatalytic carbon dioxide reduction over iron tungstate/covalent organic framework heterojunctions by the induced unified adsorption and reduction sites. *J. Colloid. Interface Sci.* **2026**, *701*, 138770. https://doi.org/10.1016/j.jcis.2025.138770.
70. Jiang, Y.; Li, Y.; Wang, G.; Huo, Z.; Shao, L.-H.; Wang, Y.; Dong, H.; Zhang, F.-M. Plasmonic Bi/COF Nanoheterojunction for Enhanced Artificial Photosynthetic CO_2 Reduction. *Inorg. Chem.* **2026**, *65*, 1264–1273. https://doi.org/10.1021/acs.inorgchem.5c04695.
71. Zhao, Y.; Wu, Z.; Cheng, Y.-Z.; Yu, X.; Li, Y.; Sui, Z.; Wang, W.; Xia, M.; Chen, Q. Enhancing the photocatalytic CO_2 reduction reaction efficiency of covalent organic frameworks through the integrating of localized surface plasmon resonances. *Appl. Catal. B Environ. Energy* **2025**, *375*, 125438. https://doi.org/10.1016/j.apcatb.2025.125438.
72. Dey, A.; Mandal, T.; Barman, S.; Maji, T.K. Covalent Organic Framework and Composite as Photocatalysts Toward Sustainable CO_2 Reduction. *Angew. Chem. Int. Ed.* **2026**, *65*, e15840. https://doi.org/10.1002/anie.202515840.
73. Li, X.-G.; Li, J.; Chen, J.; Rao, L.; Zheng, L.; Yu, F.; Tang, Y.; Zheng, J.; Ma, J. Porphyrin-based covalent organic frameworks from design, synthesis to biological applications. *Biomater. Sci.* **2024**, *12*, 2766–2785. https://doi.org/10.1039/D4BM00214H.

74. Dalapati, S.; Addicoat, M.; Jin, S.; Sakurai, T.; Gao, J.; Xu, H.; Irle, S.; Seki, S.; Jiang, D. Rational design of crystalline supermicroporous covalent organic frameworks with triangular topologies. *Nat. Commun.* **2015**, *6*, 7786. https://doi.org/10.1038/ncomms8786.
75. Yang, S.; Chen, Z.; Zou, L.; Cao, R. Construction of Thiadiazole-Linked Covalent Organic Frameworks via Facile Linkage Conversion with Superior Photocatalytic Properties. *Adv. Sci.* **2023**, *10*, 2304697. https://doi.org/10.1002/advs.202304697.
76. Vyas, V.S.; Haase, F.; Stegbauer, L.; Savasci, G.; Podjaski, F.; Ochsenfeld, C.; Lotsch, B.V. A tunable azine covalent organic framework platform for visible light-induced hydrogen generation. *Nat. Commun.* **2015**, *6*, 8508. https://doi.org/10.1038/ncomms9508.
77. Chen, B.; Li, Y.; Yang, L.; Zhang, B.; Wang, H. Synergistic Effect of Pt/Co Dual Clusters on Covalent Organic Frameworks for Highly Selective Photocatalytic CO_2 Reduction to Ethylene. *Catalysts* **2026**, *16*, 401. https://doi.org/10.3390/catal16050401.
78. Lin, Y.; Lai, X.; Huang, G.; Luo, J.; Chen, Q.; Huang, G.; Bi, J. Spatial Confinement of Pd Nanoclusters in Pyrene-Based Covalent Organic Frameworks for Boosting Photocatalytic CO_2 Reduction. *Chem. Eur. J.* **2025**, *31*, e202500766. https://doi.org/10.1002/chem.202500766.
79. Huang, X.; Chen, Y.; Xie, X.; Song, T. Covalent Organic Frameworks with Tunable Bridge Positions for Photocatalytic CO_2 Reduction to Propylene Under Visible Light Illumination. *Small* **2025**, *21*, 2408817. https://doi.org/10.1002/smll.202408817.
80. Wu, Y.; Hu, Q.; Chen, Q.; Jiao, X.; Xie, Y. Fundamentals and Challenges of Engineering Charge Polarized Active Sites for CO_2 Photoreduction toward C2 Products. *Acc. Chem. Res.* **2023**, *56*, 2500–2513. https://doi.org/10.1021/acs.accounts.3c00373.
81. Roudsari, B.D.; Hasannia, S.; Kazemeini, M. Selective photocatalytic reduction of CO_2 to CO mediated by atomically dispersed Cu-anchored upon hollow covalent organic frameworks. *J. CO2 Util.* **2025**, *102*, 103282. https://doi.org/10.1016/j.jcou.2025.103282.
82. Gao, F.; Liu, G.; Chen, A.; Hu, Y.; Wang, H.; Pan, J.; Feng, J.; Zhang, H.; Wang, Y.; Min, Y.; et al. Artificial photosynthetic cells with biotic–abiotic hybrid energy modules for customized CO_2 conversion. *Nat. Commun.* **2023**, *14*, 6783. https://doi.org/10.1038/s41467-023-42591-x.
83. Zhou, W.; Wang, X.; Zhao, W.; Lu, N.; Cong, D.; Li, Z.; Han, P.; Ren, G.; Sun, L.; Liu, C.; et al. Photocatalytic CO_2 reduction to syngas using metallosalen covalent organic frameworks. *Nat. Commun.* **2023**, *14*, 6971. https://doi.org/10.1038/s41467-023-42757-7.
84. Ma, S.; Chen, D.; Yuan, K.; Du, G.; Li, F.; Zhu, Y. Asymmetric charge sites for the photoreduction of CO_2 into high-value C_{2+} products. *Coord. Chem. Rev.* **2026**, *564*, 218086. https://doi.org/10.1016/j.ccr.2026.218086.
85. Hirani, Z.; Schweitzer, N.M.; Vitaku, E.; Dichtel, W.R. A Phenazine-Based Two-Dimensional Covalent Organic Framework for Photochemical CO_2 Reduction with Increased Selectivity for Two-Carbon Products. *Angew. Chem. Int. Ed.* **2025**, *64*, e202502799. https://doi.org/10.1002/anie.202502799.
86. Fu, P.; Meng, B.; Hu, Q.; Wei, J.; Yue, Q.; Sun, M.; Xu, Q.; Liu, X.; Xi, S.; Yin, W.; et al. Covalently Tethering Atomically Precise Au25 Nanoclusters onto Covalent Organic Framework for Visible-light Driven CO_2 Reduction. *Research* **2026**, *9*, 1152. https://doi.org/10.34133/research.1152.
87. Dong, J.P.; Xu, Y.; Yao, L.; Wang, L.; Li, G.; Wang, R.; Zang, S.Q. New Strategy for Cluster-Based Covalent Organic Framework: Thermally Induced Covalent Crosslinking of Highly Stable Copper Clusters. *Adv. Sci.* **2025**, *12*, e07510. https://doi.org/10.1002/advs.202507510.
88. He, C.; Liu, W.; Zhu, E.; Zhu, Y.; Chen, C. Directing robust built-in electric fields via imine linkage orientation in COFs for efficient dehydrogenative organic transformation coupled with H_2O_2 photosynthesis. *Chem. Sci.* **2026**, *17*, 3075–3083. https://doi.org/10.1039/D5SC08299D.
89. Zhang, Q.; Gao, S.; Guo, Y.; Wang, H.; Wei, J.; Su, X.; Zhang, H.; Liu, Z.; Wang, J. Designing covalent organic frameworks with Co-O_4 atomic sites for efficient CO_2 photoreduction. *Nat. Commun.* **2023**, *14*, 1147. https://doi.org/10.1038/s41467-023-36779-4.
90. Fang, S.; Zhu, X.; Liu, X.; Gu, J.; Liu, W.; Wang, D.; Zhang, W.; Lin, Y.; Lu, J.; Wei, S.; et al. Uncovering near-free platinum single-atom dynamics during electrochemical hydrogen evolution reaction. *Nat. Commun.* **2020**, *11*, 1029. https://doi.org/10.1038/s41467-020-14848-2.
91. Cao, L.-L.; Liu, X.; Shen, X.; Wu, D.; Yao, T. Uncovering the Nature of Active Sites during Electrocatalytic Reactions by In Situ Synchrotron-Based Spectroscopic Techniques. *Acc. Chem. Res.* **2022**, *55*, 2594–2603. https://doi.org/10.1021/acs.accounts.2c00212.
92. Fei, X.; Zhang, L.; Yu, J.; Zhu, B. DFT Study on Regulating the Electronic Structure and CO_2 Reduction Reaction in BiOBr/Sulphur-Doped G-C_3N_4 S-Scheme Heterojunctions. *Front. Nanotechnol.* **2021**, *3*, 698351. https://doi.org/10.3389/fnano.2021.698351.
93. Wang, Y.; Sun, Y.; Liu, X.; Dong, F. Predicting and understanding photocatalytic CO_2 reduction reaction with IR spectroscopy-based interpretable machine learning framework. *PNAS Nexus* **2024**, *3*, pgae339. https://doi.org/10.1093/pnasnexus/pgae339.

94. Yu, H.; Chen, F.; Li, X.; Huang, H.; Zhang, Q.; Su, S.; Wang, K.; Mao, E.; Mei, B.; Mul, G.; et al. Synergy of ferroelectric polarization and oxygen vacancy to promote CO_2 photoreduction. *Nat. Commun.* **2021**, *12*, 4594. https://doi.org/10.1038/s41467-021-24882-3.
95. Sun, L.; Su, H.; Chen, Z.; Orbell, W.; Liang, G.; Wang, W.; Wang, L.; Yang, J.; Liu, Q.; Li, J. Atomic Interlayer Mo–N4 Sites Enable Rapid Charge Transfer and Efficient CO_2 Photoreduction. *Adv. Sci.* **2026**, *13*, e75217. https://doi.org/10.1002/advs.75217.
96. Xiao, Z.; Feng, Q.; Zheng, Z.; Guo, W.; Zhang, X.; Wang, Y. Continuous High-Spin Orbital Coupling for Enhanced CO_2 Photoreduction With H_2O in Covalent Organic Frameworks. *Angew. Chem. Int. Ed.* **2026**, *65*, e5485021. https://doi.org/10.1002/anie.5485021.
97. Yu, M.; Chen, W.; Lin, Q.; Li, L.; Liu, Z.; Bi, J.; Yu, Y. Electrostatic Confinement-Induced Excited Charge Transfer in Ionic Covalent Organic Framework Promoting CO_2 Reduction. *Angew. Chem. Int. Ed.* **2025**, *64*, e202418422. https://doi.org/10.1002/anie.202418422.
98. Xue, R.; Zhang, R.; Yin, L.-h.; Liu, Y.-s.; Lv, Y.; Wu, X.-y.; Guo, J.-x. Three-dimensional covalent organic frameworks for photocatalysis. *Coord. Chem. Rev.* **2026**, *560*, 217879. https://doi.org/10.1016/j.ccr.2026.217879.
99. Chang, S.; Feng, Y.; Zhao, Y.; Fu, Y.; Jia, H.; Gao, Y.; Zhang, F.; Ma, R.; Lu, X.; Fan, M.; et al. Fabrication of p–n Heterostructured Photocatalysts with Triazine-Based Covalent Organic Framework and CuInS2 for High-Efficiency CO_2 Reduction. *ACS Appl. Mater. Interfaces* **2024**, *16*, 13839–13848. https://doi.org/10.1021/acsami.3c19525.
100. Wang, J.; Wang, L.; Zhang, D.; Wang, Y.; Li, J.; Zhou, F.; Huang, J.; Liu, Y.-N. Covalently connected core–shell NH2-MIL-125@COFs-OH hybrid materials for visible-light-driven CO_2 reduction. *J. Colloid. Interface Sci.* **2023**, *637*, 1–9. https://doi.org/10.1016/j.jcis.2022.12.154.
101. Mao, J.; Wang, L.; Qu, S.; Zhang, Y.; Huang, J.; She, H.; Bai, Y.; Wang, Q. Defect Engineering in CuSx/COF Hybridized Heterostructures: Synergistic Facilitation of the Charge Migration for an Efficacious Photocatalytic Conversion of CO_2 into CO. *Inorg. Chem.* **2022**, *61*, 20064–20072. https://doi.org/10.1021/acs.inorgchem.2c03481.
102. Lin, H.; Liu, Y.; Wang, Z.; Ling, L.; Huang, H.; Li, Q.; Cheng, L.; Li, Y.; Zhou, J.; Wu, K.; et al. Enhanced CO_2 Photoreduction through Spontaneous Charge Separation in End-Capping Assembly of Heterostructured Covalent-Organic Frameworks. *Angew. Chem. Int. Ed.* **2022**, *61*, e202214142. https://doi.org/10.1002/anie.202214142.
103. Yang, R.; Chen, Q.; Huang, G.; Bi, J. Interfacial engineering of novel inorganic-organic β-Ga_2O_3/COF heterojunction for accelerated charge transfer towards artificial photosynthesis. *Environ. Res.* **2023**, *216*, 114541. https://doi.org/10.1016/j.envres.2022.114541.
104. Hao, S.; Yan, X.; Yin, H.; Wang, H.; Yu, J.; Bai, L. Confined Polyhydroxylated C60 in Porphyrin COF Nanopore as Nanoreactor for CO_2 Photoreduction. *Trans. Tianjin Univ.* **2026**, *32*, 531–543. https://doi.org/10.1007/s12209-026-00494-0.
105. Zhao, W.; Li, J.; Li, K.; Jiao, J.; Liu, S.; Yang, J.; Frogley, M.D.; Peng, Y.; Wang, Y.; Wang, H.; et al. Enhancing CO_2 Photoreduction Efficiency Through Improved Interaction Enabled by a Decorated Covalent-Organic Framework. *Angew. Chem. Int. Ed.* **2025**, *64*, e202510550. https://doi.org/10.1002/anie.202510550.
106. Liu, T.; Fu, Y.-M.; Meng, X.; Xue, L.; Wang, H.-N.; Su, Z.-M. Design of titanium-oxide cluster-based metal-covalent organic frameworks for efficient photocatalytic CO_2 reduction. *Dalton Trans.* **2025**, *54*, 15537–15543. https://doi.org/10.1039/D5DT01871D.
107. Hou, Y.; Ma, H.; Zhu, D.; Li, R.; Zhao, Z.; Li, C.-X.; Cui, C.-X.; Wang, J.-C. Noble metal-free porphyrin covalent organic framework layer for CO_2 photoreduction to CO. *Dalton Trans.* **2025**, *54*, 405–413. https://doi.org/10.1039/D4DT02658F.
108. Dong, H.; Che, H.-T.; Bai, L.-W.; Zhang, N.-N.; Tian, Y.-Q.; Li, B.-Z.; Wang, Y.; Zhang, X.; Zhang, F.-M. Benzotrithiophene-Based Covalent Organic Frameworks with Rhenium Modified for Artificial Photosynthetic CO_2 Reduction. *Inorg. Chem.* **2024**, *63*, 24421–24428. https://doi.org/10.1021/acs.inorgchem.4c04599.
109. Fu, Y.; Gao, Y.; Jia, H.; Zhao, Y.; Feng, Y.; Zhu, W.; Zhang, F.; Argyle, M.D.; Fan, M. Rational engineering of triazine-benzene linked covalent-organic frameworks for efficient CO_2 photoreduction. *Green Energy Environ.* **2025**, *10*, 804–812. https://doi.org/10.1016/j.gee.2024.07.002.
110. Xue, H.; Yin, C.; Xiong, S.; Yang, J.; Wang, Y. One-pot Synthesis of Metal-coordinated Covalent Organic Frameworks for Enhanced CO_2 Photoreduction. *ACS Appl. Mater. Interfaces* **2022**, *14*, 49672–49679. https://doi.org/10.1021/acsami.2c12303.
111. Yang, Z.; Sun, Y.; Liu, H.; Li, Z.; Huang, B.; Cheng, H. In Situ DRIFTS in Photocatalytic CO_2 Reduction: Basic Principle and Current Progress. *J. Phys. Chem. C* **2026**, *130*, 8881–8906. https://doi.org/10.1021/acs.jpcc.6c01504.
112. Chakraborty, S.; Kaur, J.; Mehtab, A.; Peter, S.C. In situ and operando characterization of photo/photothermocatalytic CO_2 reduction. *Chem. Catal.* **2026**, *6*, 101684. https://doi.org/10.1016/j.checat.2026.101684.

113. Li, S.; Xue, Q.; Zhang, T. Linkage transformation in covalent organic frameworks from dynamic precursors to robust skeletons. *Chem. Sci.* **2026**, *17*, 16069–16089. https://doi.org/10.1039/D6SC04251A.
114. Waller, P.J.; Lyle, S.J.; Osborn Popp, T.M.; Diercks, C.S.; Reimer, J.A.; Yaghi, O.M. Chemical Conversion of Linkages in Covalent Organic Frameworks. *J. Am. Chem. Soc.* **2016**, *138*, 15519–15522. https://doi.org/10.1021/jacs.6b08377.

Disclaimer/Publisher's Note: The statements, opinions and data contained in all publications are solely those of the individual author(s) and contributor(s) and not of MDPI and/or the editor(s). MDPI and/or the editor(s) disclaim responsibility for any injury to people or property resulting from any ideas, methods, instructions or products referred to in the content.